Numerical Modelling of Wind Storms in the Lower Great Lakes

by

Laura Chandler

A thesis
presented to the University of Waterloo
in fulfillment of the
thesis requirement for the degree of
Masters of Mathematics
in
Applied Mathematics (Water)

Waterloo, Ontario, Canada, 2018

I hereby declare that I am the sole author of this thesis. This is a true copy of the thesis, including any required final revisions, as accepted by my examiners.

I understand that my thesis may be made electronically available to the public.

Abstract

Convective storms are incredible meteorological events; the impact of just one storm can be extreme and widespread. On July 21 1998, a convective storm formed west of Lake Michigan, moving quickly across the lower Great Lakes region. The damage due to this storm was widespread, with one of the most impacted areas being Ontario's Rondeau Park on the north shore of Lake Erie, where over half of the trees in the park fell due to wind stress. In this thesis, wind speed and wind gust data from Erieau, Ontario and Detroit, Michigan are used to provide a climatology of typical wind speeds in the region, determining that high wind speeds are rare and short-lived during the summer months of June, July, and August. Wind speed, gust speed, radar, and reanalysis data are analyzed to characterize the 1998 storm, providing evidence that the storm in question is exceptional in both longevity as well as high sustained wind and gust speeds. Within the summer months, the existence of such a wind event is found to be uncommon.

The Weather Research and Forecasting (WRF) model is used to perform simulations of the storm. A fine resolution simulation is found to capture the general shape and intensity of the storm and is used to provide further characteristics of the simulated storm. Large convective available potential energy (CAPE) and significant low-level shear are found to be present in the domain during the formation and propagation of the storm. The storm grows to have a radius of 250 km and travels over 1000 km before eventually dissipating. Over Rondeau Park, an additional downburst forms in the region as the main front of the storm passes, acting to heighten and lengthen the effects of observed wind at the park. An additional coarse resolution simulation is performed to determine the effects of resolution and convective parameterization on storm propagation and general wind speeds. It is found that the coarser resolution and parameterization of convective up- and downdrafts act to dampen the wind speeds experienced at the park and decrease the areal extent of the storm. To determine the sensitivity of the storm to Lake Erie and Lake St. Clair, a simulation is performed in which both lakes are replaced by forests. This simulation shows that the wind speed and general shape of the storm is greatly enhanced by lakes over a large region and particularly at Rondeau Park.

Acknowledgements

Firstly, thank you to my supervisors, Marek Stastna and Michael Waite, whose kindness and guidance is much appreciated. Thank you to my thesis committee, Chris Fletcher and Francis Poulin, in addition to Marek and Mike, for taking the time to read and review my work. An additional thank-you to Francis for introducing me to the field of fluid mechanics.

Thank you to the communities that this degree has enabled me to be a part of. To Applied Math, thank you for teaching me that math is more than just numbers. To the lab, particularly those who have gone above and beyond to make me feel like this is a place I should be, thank you for your friendship and mentorship. To FemPhys, thank you for lifting me up, for teaching me about everything from gardening to community to intersectional feminism, for being exactly what this university needs, and so much more.

And now we get personal! Thank you to my parents, forever and always, for supporting me in every ridiculous endeavour I get up to. Thank you to my grandmothers for being such strong role models in my life and for teaching me to "take shit from nobody". Thank you to my brother for being my best pal since day one. Thank you to my friends near and far for hearing my cries and listening to my rants. Thank you to the Sioui family for being my Ontario family while mine is so far away. Thank you to Jeremy for showing me nothing but love and support in this journey.

Thank you to the ground and sky and trees and seas for inspiring me every single day! As I work to appreciate and understand how the earth works, I also acknowledge the complex history that people have with this land. This thesis was researched in its entirety at the University of Waterloo which resides on traditional territory- particularly that of the Anishinaabe, Haudenosaunee, and Attawandaron peoples.

Dedication

To my family, for always encouraging my love of science and my love of art.

Table of Contents

List of Tables

List of Figures

Chapter 1

Introduction

Atmospheric convection in the summertime can produce incredible and severe storms. They can be immensely powerful, impacting both nature and society over extremely large regions. On July 21 1998, a strong convective storm moved through the lower Great Lakes. Forming west of Lake Michigan and traveling eastwards at a rate of 100 km/h, the storm drastically picked up speed over Lake Michigan and continued onward over Lake Erie. In just one evening, severe wind damage was reported throughout Wisconsin, Michigan, Ontario, Ohio, and Pennsylvania. In particular, high winds were observed at Rondeau Park, Ontario, where over half the trees in the park suffered from fatal wind damage (Larson and Waldron, 2000). The extent of damage that occurred in this region is the motivation behind the work in this thesis.

Convective wind storms arise in the presence of high surface humidity and buoyant instability such as that due to near-surface heating. Features like this are common on a hot summer afternoon. When a warm, moist air parcel near the surface is lifted, it cools, causing water vapour to eventually condense into cloud water and rain. When condensation occurs, latent heat is released and the air parcel gets warmer. Thus, the air parcel becomes even more buoyant and is likely to rise higher into the atmosphere, causing convection (Rogers, 1976). It is difficult to predict when a turbulent or mechanical process will provide enough energy for air parcels to overcome convective inhibition and grow into deep convective storms. However, once triggered, convection has the potential to be very intense and act as a source of energy for strong wind events such as downbursts (Emanuel, 1994), where a strong downdraft accelerates downwards, sending straight-line surface winds radially from its source (Fujita, 1978).

Convective wind storms occur over a large part of the year in many locations around

the globe, varying greatly in size and length (Fujita, 1978). Multiple climatologies determine that the summer months of May-August are the highest frequency months and the lower Great Lakes are the highest frequency corridor in the greater United States for both highly damaging and derecho-producing convective wind storms (Bentley and Mote, 1998; Coniglio et al., 2004; Johns and Hirt, 1987; Schoen and Ashley, 2011). A derecho is a long-lived large scale convective wind storm that consists of multiple downburst clusters (Johns and Hirt, 1987). Within the lower Great Lakes corridor in particular, nontornadic convective wind storms can often prove to be more fatal and damaging than those that produce tornadoes, due to their higher frequency of occurrence and greater spatial extent (Schoen and Ashley, 2011).

1.1 Numerical Weather Prediction

In order to further investigate wind storms, numerical weather prediction (NWP) models such as the Weather Research and Forcasting (WRF) model, the Global Forecast System (GFS), the North American Mesoscale (NAM) model, and the European Centre for Medium-Range Weather Forecasts (ECMWF) model can be used to perform case studies of specific storm events. Case studies of convective storms have been compared to observational data to determine model accuracy (Coniglio et al., 2013; Litta et al., 2012). When modelling convective storms, the resolution of the simulation is important to consider, especially when determining if using convective parameterization is an appropriate approach (Arakawa, 2004). By varying grids from 1-12 km spacing without convective parameterization, it has been shown that a 4 km grid resolution is sufficient in approximately representing mesoscale squall lines (Weisman et al., 1997). Using the WRF model in particular, it was shown that simulations with horizontal grid spacing finer than 4 km without a convective parameterization will more accurately represent the time, location, and structure of mesoscale convective storms when compared to a simulation with a 10 km resolution that uses convective parameterization (Done et al., 2004). This thesis compares wind speeds over an entire month as well as storm-specific dynamics of simulations with resolutions of 2 km and 10 km. Since the coarser grid employs convective parameterizations, this determines the effects of resolution and parameterization on both seasonal and storm dynamics. Both simulations are compared to wind speed observations from multiple stations to determine the accuracy of the simulations and potential challenges with wind speed sampling.

In addition, NWP models can be used to measure the sensitivity of an atmospheric event to a particular topographic feature by modifying the feature in the simulation. For instance,

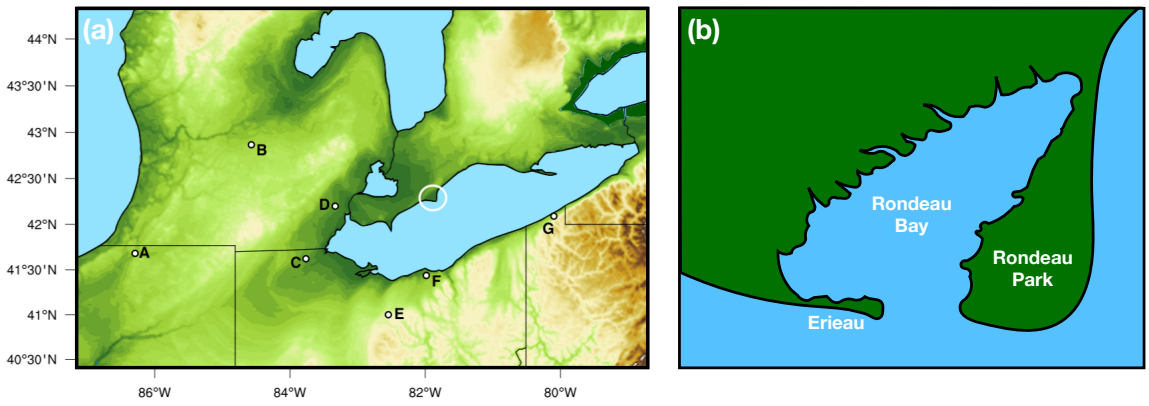

Figure 1.1: The domain of interest: (a) The larger region of storm propagation with locations of weather stations from which data is acquired, with the circled region denoting Rondeau Park in subfigure (b). (b) The location of Rondeau Bay, Rondeau Park, and the Erieau weather station.

the effects of the Coastal Mountain Range on a California flood (Colle and Mass, 2000), the Rocky Mountains on flooding events in Alberta (Flesch and Reuter, 2012), the Sierra Nevada on cold front formation (West and Steenburgh, 2011), differing lake-ice conditions on a cold-air outbreak over the Great Lakes (Wright et al., 2013), the Uinta Mountains on a downslope wind event in Utah (Lawson and Horel, 2015), farmland versus urban land use on warm lake breezes in Chicago (Sharma et al., 2017), and lakes on climate patterns near the Tibetan Plateau (Zhu et al., 2017) have all used this approach to determine the sensitivity of a meteorological event to a certain feature. Others have compared wind speed observations to NWP simulations for investigating how wind gusts affect sea drag (Babanin and Makin, 2008) or determining spatial optimizations for producing appropriate wind gusts during Swiss winter wind storms (Stucki et al., 2016). This thesis uses land-use modification to determine storm-scale sensitivity to lakes by simulating a storm in which certain lakes are replaced by forest.

1.2 Region and Storm of Interest

Rondeau Park, the domain of interest, is located on the north shore of Lake Erie, at 42.2606°N, -81.8597°W (Figure 1.1). It is an 8 km long sandspit into Lake Erie, measuring 0.5 km wide in the north and 3.1 km at the widest area in the south (Tanentzap et al., 2011).

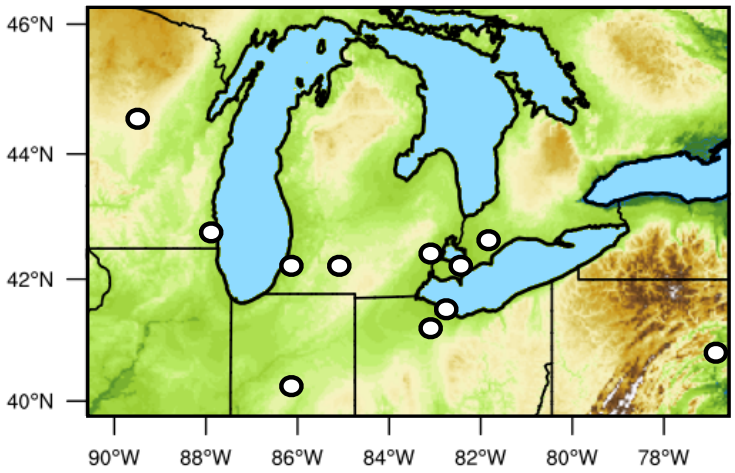

Figure 1.2: The location of all daily newspapers in which the storm was the front-page story on July 22 1998.

Rondeau Park contains a large Carolinian forest, campgrounds, and a cottage community. To the southwest of the park is a large marsh, Rondeau Bay, and a continuation of the sandspit, Erieau, which nearly closes off the bay. To the east is open lake. The nearby lake has a hydrodynamically smooth surface, and hence provides a large fetch with sufficient room for the wind speeds to pick up in the absence of surface roughness and vegetation. A nearby weather station is located across Rondeau Bay at Erieau, at which wind speed, wind direction, and temperature data is collected by Environment and Climate Change Canada (ECCC). This data, along with wind speed data from the various locations shown in Figure 1.1(a), will be used for further analysis of the storm.

In the late afternoon of July 21, 1998, a large summer convective storm formed in the southern Great Lakes, moving across the region at a rate of approximately 100 km/h. Gusts of up to 34 m/s were recorded along the path of the storm. The societal impact of the storm was vast, making the front page of at least 11 daily newspapers ranging from Wood, Wisconsin to Hazleton, Pennsylvania, 1200 km apart. To show how great an area this is, the location of every known newspaper in which the storm was the front-page story on July 22 1998 is shown in Figure 1.2. Referencing these newspapers, the storm was referred to as "Summer's Fury" and "the Storm of the Century." Severe damage from the storm was reported over a span of over 1000 km from Wisconsin to Pennsylvania, with the midpoint close to Rondeau Park. Damages included the widespread flattening of trees and

crops, storm-related fires, overturning trucks, widespread and lengthy power outages, wild waves on Lake Erie and Lake St. Clair causing boats to capsize, and trees falling on cars and homes causing numerous accounts of people becoming trapped inside cars and houses. There was one direct death due to the storm in Detroit, Michigan.

The storm crossed Rondeau Park near 00:00 UTC on July 22 1998, causing damage and destruction to trees and cottages in the area. In North America, the potential for wind damage such as uprooted trees is assumed to begin when near-surface winds reach 25 m/s (Doswell, 1993), wind speeds often associated with downbursts from convective summer storms such as this one (Fujita, 1978). Sampling of the forest stand within the park (Larson and Waldron, 2000) took place on June 9th and August 3rd 1998, and found that 51% of the sampled trees had fallen or broken during the storm. The largest trees, with mean diameter of 47 cm, took the most damage during the storm, reducing the mean diameter of the forest by approximately 14 cm and decreasing canopy cover from 70% to 30-40%.

1.3 Format of Thesis

This work looks at the wind storm of July 21-22 1998 in detail: where it fits within the climatology of the region, its formation and propagation characteristics, and its sensitivity to surface conditions in the area. Chapter 2 describes convective storms in general: atmospheric conditions appropriate for their formation as well as typical storm processes. The equations of motion in the atmosphere and how they are represented within the WRF model are outlined, along with the data sources, model parameterizations, simulation descriptions, and adjustments made to the model.

Climatology analysis is performed in Chapter 3 on wind speed data from the Erieau station provided by ECCC, located near Rondeau Park across Rondeau Bay, and for wind speed data from the Detroit Metropolitan Regional Airport in Michigan provided by National Oceanic and Atmospheric Administration (NOAA). A number of NOAA stations are used to analyze the propagation of the storm. Using sustained wind and gust speed observations provided by NOAA, gust strength at ECCC's Erieau is approximated during high wind events. Using North American Regional Reanalysis (NARR) data, it can be seen that the storm of July 21-22 1998 was likely caused by a strong low-pressure system traveling eastward over the northern Great Lakes, causing rising air, a strong change in humidity, and strong geostrophic winds over the southern Great Lakes. These conditions are similar to those determined as favourable for severe thunderstorm development (Johns, 1993; Johns and Doswell, 1992).

To learn more about the storm, high resolution simulations of the storm are performed with WRF (Skamarock et al., 2008) using NARR-produced initial and boundary conditions, presented in Chapter 4. Simulation data is analyzed to compare to the observed wind speed, wind direction, temperature at the location of the Erieau station. Likewise, outputted reflectivity is compared with NOAA radar data. Wind speed histograms for the observed and simulated month of July are analysed and compared with the appropriate Weibull distributions. Further characterizations are made of the storm based on simulated CAPE, surface pressure, relative humidity, and winds. Sensitivity analysis is performed for multiple grid resolutions to determine the effects of convective parameterization on storm characteristics. To determine the effects of Lake Erie and Lake St. Clair on the wind speed of the storm, an additional simulation is run in which both lakes are replaced by forest. Finally, Chapter 5 summarizes the outcomes of this thesis and discusses real world implications with regards to storm damage, and outlines possible directions for future work.

Chapter 2

Technical Background and Methods

Due to the nature of the atmosphere, fluid parcels must be considered as a mixture of dry air and water vapour. The latent heat released by saturated air that forms condensation has an influence on a number of dynamics, including the formation of convective storms. Along with latent heat, the role of buyoancy is incredibly important in the discussion of these storms. Both of these qualities of the atmosphere can be used to discuss the convective available potential energy (CAPE) of an air parcel. The presence of CAPE, along with mechanical forces, provide conditions favourable for storm development. In addition, the presence of a vertical shear is important in storm propagation. These atmospheric features are discussed in Section 2.1. To describe the atmospheric motions mathematically, the Euler Equations, along with additional mathematical tools, are outlined in section 2.2.

To look at climatological wind speeds, atmospheric features, and storm dynamics in the lower Great Lakes, a number of observational sources are used. The wind speed data, radar data, and reanalysis data used in this thesis are outlined in section 2.3. The WRF model, described in Section 2.4, is used to numerically model atmospheric movements. It uses the compressible Euler equations adjusted to include moisture and terrain-following pressure coordinates. Using WRF, a set of simulations are performed to look at seasonal wind speeds and local storm dynamics. The set-up of simulations, along with parameterizations and modifications, are described in Section 2.5.

2.1 Review of a Convective Storm Environment

To determine atmospheric conditions needed for severe weather to occur, it is important to consider the atmosphere as a mixture of dry air and water vapour. When water evaporates

to become vapour, heat is required since the kinetic energy of vapour exceeds that of a liquid at the same temperature. The latent heat of vaporization is the heat required to convert a unit mass of liquid to vapour, with temperature and pressure held constant. There are a variety of ways in which moist air can reach saturation: moist air can be cooled diabatically at constant pressure, cooled adiabatically by lifting, or water can be evaporated directly into the moist air, thus cooling the air (Rogers, 1976).

When a parcel of air is moved throughout the atmosphere by mechanical forces, the air parcel may change temperature, pressure, specific volume (the ratio of volume to mass), and/or transfer heat. Many temperature changes in the atmosphere can be approximated as an adiabatic process: one that occurs without transfer of heat. In this case, energy is only transferred as work. Instead of the transfer of heat, often the pressure or specific volume will change when the temperature of a fluid parcel changes (Rogers, 1976). The potential temperature (θ) is a useful variable of state that is conservative with respect to an adiabatic process:

$$\theta = T(\frac{p_0}{p})^k, \tag{2.1}$$

where T is temperature, p is pressure, p_0 is standard atmospheric pressure, and $k = (c_p - c_v)/c_p = 0.286$ is a constant dependent on the specific heat capacity of dry air at a constant volume (c_v) and constant pressure (c_p). The potential temperature is the temperature that a parcel of air, with given initial starting temperature T and pressure p, would have if it were subjected to an adiabatic compression or expansion to a final pressure of $p_0 = 1000\ mb$, or standard atmospheric pressure at the surface (Rogers, 1976). In addition to an adiabatic process, a pseudoadiabatic process can occur for lifted parcels after air reaches saturation: the condensation is assumed to turn into rain immediately and drop out, the air parcel is heated by latent heating, and the temperature decreases more slowly than for adiabatic lifting.

An additional variable that provides insight into how water vapour in air effects atmospheric dynamics is the virtual temperature T_v of a moist air parcel. This is the temperature that a parcel of dry air would be if it has the same pressure and density as the moist air parcel (Rogers, 1976). With regards to the equation of state for dry air, the virtual temperature provides a correction factor to the temperature such that the same equation of state can be used for moist air as well. The equation of state is:

$$p\alpha = R'T_v, \tag{2.2}$$

where α is the specific volume, R' is the individual gas constant, and $T_v = T(1 + 0.6w)$, where w is the mass of water vapour per unit mass of dry air.

Buoyancy in the atmosphere plays a key role in the development of atmospheric convection. If a parcel of air with volume V, potential temperature θ, and density ρ displaces an equal volume of air with potential temperature θ' and density ρ', the parcel will experience upward and downward forces of $\rho' gV$ and ρgV respectively (Rogers, 1976). Thus the buoyant force per unit mass is:

$$F_B = g(\frac{\rho' - \rho}{\rho}) = g(\frac{\theta' - \theta}{\theta}), \tag{2.3}$$

where g is the acceleration due to gravity. If the air parcel is warmer than its surroundings, it will experience an upwards buoyant force.

As an unsaturated air parcel is lifted due to an adiabatic process, it will decrease in temperature at a constant rate called the adiabatic lapse rate (Rogers, 1976):

$$\Gamma = -dT/dz = g/c_p = 9.8°C/km. \tag{2.4}$$

Referencing Figure 2.1, this can be seen as the temperature of the air parcel below the lifting condensation level (LCL), or the straight portion of the red line. However, when lifted upwards, a fully saturated parcel will decrease in temperature at a pseudoadiabatic rate; the latent heat released during condensation will warm the parcel such that this rate is less than the dry adiabatic lapse rate, shown in Figure 2.1 as the curved red line between the LCL and the level of neutral buoyancy (LNB).

A parcel in the atmosphere is stable if, after a vertical displacement, it is restored to its original location. It is unstable if the parcel continues to move away from its original point. Whether a parcel in the atmosphere is stable or not depends on two things: the rate of change of the temperature of the parcel with height and the rate of change of the temperature of the surrounding atmosphere with height. If the temperature of the environment decreases with height at a faster rate than the temperature of the parcel, then a parcel displaced a certain height will accelerate upwards (Lin, 2007).

The lower layer of the atmosphere is well-mixed. Parcels of air from this layer are randomly forced upwards by mechanical forces triggered by mechanisms such as synoptic fronts or localized regions of excess surface heating (Stull and Ahrens, 2000). Figure 2.1 shows the process in which a parcel of air undergoes convection. If a parcel of unsaturated air is lifted, its temperature follows a dry adiabatic path until it condenses at the LCL. At this point, if it continues lifting, the parcel will warm due to the release of latent heat as condensation is released, and thus follows a pseudoadiabat above this level. If the parcel continues to lift, it will reach a height in which it has the same temperature as its

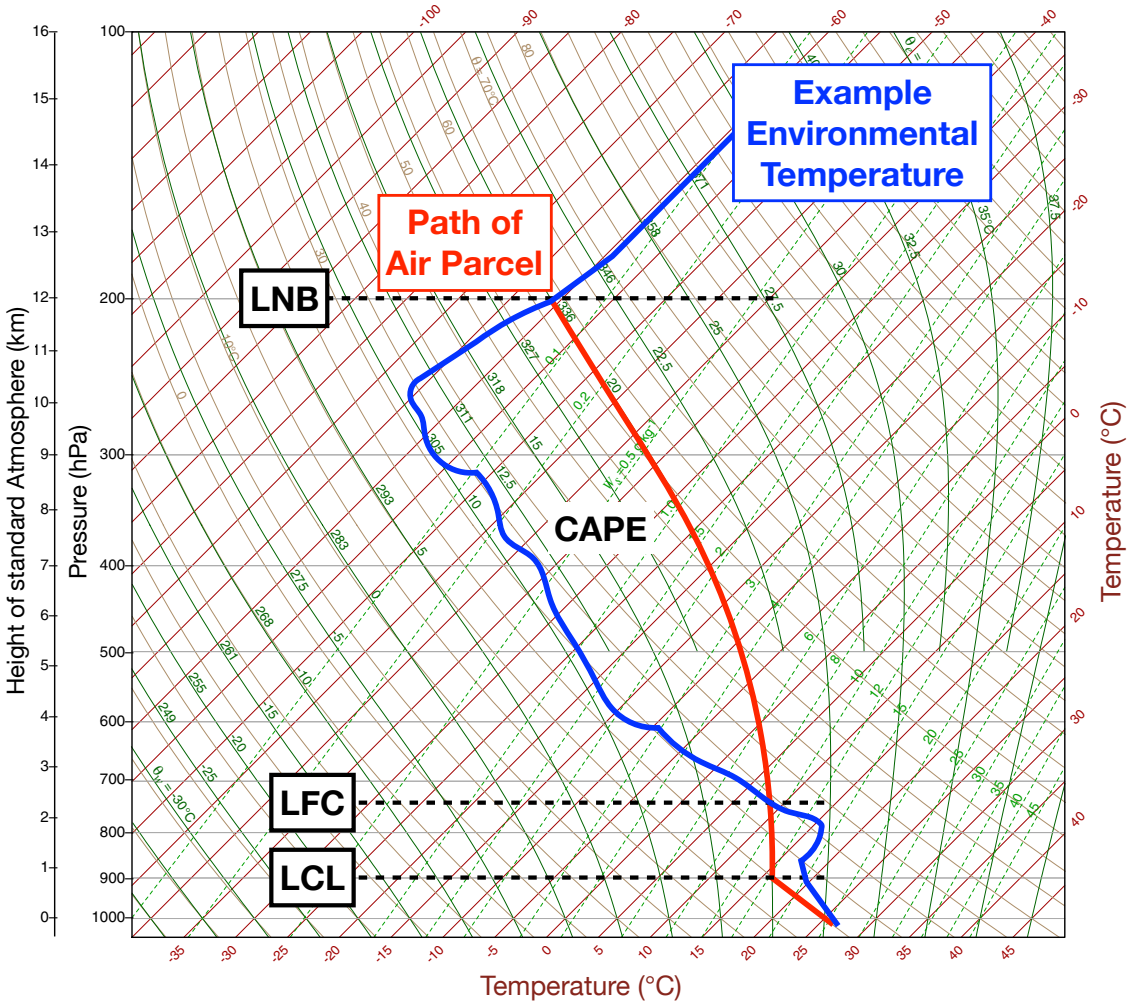

Figure 2.1: A Skew T - ln p plot showing the path of an air parcel's temperature (red) and an example environmental temperature (blue) describing the processes necessary for convective activity. Horizontal dashed black lines denote the lifting condensation level (LCL), level of free convection (LFC), and the level of neutral buoyancy (LNB). Original axes courtesy of Jennifer Adams, COLA.

surroundings, known as the level of free convection (LFC). If lifted beyond this point, the parcel will be warmer than its surroundings and can rise on its own without mechanical forcing until it reaches the level of neutral buoyancy near the tropopause, between the troposphere and the stratosphere, at 8-12 km high. This is known as conditional instability:

the unsaturated parcel is stable, but once it becomes saturated and passes a certain point, the parcel becomes unstable (Lin, 2007). A phenomenon such as this would not be able to happen in a dry atmosphere due to the latent heat released once air is saturated.

Both updrafts, described above, and downdrafts are associated with convective storms. As an air parcel rises into the colder layers of the atmosphere, the parcel reaches saturation, and further lifting causes water vapour to condense into cloud water. As cloud droplets grow through microphysical processes, they eventually become larger droplets or ice particles that fall as precipitation (Stull and Ahrens, 2000). As precipitation falls into warmer sub-saturated air below the cloud, it absorbs latent heat as it changes from solid to liquid and subsequently evaporates (Emanuel, 1994). Thus, the sub-cloud air is cooled, becoming more dense, and accelerates downward as a downdraft. These descending downdrafts can hit the ground and spread out as straight-line winds.

Atmospheric convection is the vertical motion driven by latent heating and moist instability. It determines the vertical transport of heat, mass, and momentum. Due to buoyant forces activated by mechanical forces, convection will result in the conversion of potential energy to kinetic energy. The amount of potential energy available for convection, or the CAPE, is defined as the work done by the buoyancy force in lifting an air parcel from the LFC to the LNB (Rogers, 1976). The equation for the CAPE of a parcel is:

$$\text{CAPE} = \int_{z_{LFC}}^{z_{LNB}} g \left(\frac{\theta_{parcel} - \theta_{env}}{\theta_{env}} \right) dz, \tag{2.5}$$

where z_{LFC} is the height of the level of free convection, z_{LNB} is the height of the level of neutral buoyancy, θ_{parcel} is the potential temperature of the air parcel, and θ_{env} is the potential temperature of the environment. Thus, the CAPE of an air parcel can be viewed as the area between the blue and red curves in Figure 2.1 above the LFC and below the LNB. The larger the CAPE of an air parcel, the more buoyant and strong the convection will be, provided the parcel is lifted to the LFC by some mechanical forcing. There are many atmospheric scenarios that cause a larger area between the blue and red curves in Figure 2.1 and thus a larger CAPE: more moisture at the surface shifts the air parcel's LCL downwards and thus the parcel's temperature will follow a pseudoadiabat closer to the ground, a cooler environmental temperature above the LFC shifts the blue curve to the left in this region, or a larger environmental temperature gradient below the LCL, and thus a higher surface temperature, will shift the red curve to the right. CAPE values of 300 J/kg are associated with a mostly stable environment with little to no thunderstorm activity, while CAPE values of over 3500 J/kg are associated with an extremely unstable environment and severe thunderstorm activity (Stull and Ahrens, 2000).

2.1.1 Mesoscale Convective Storms

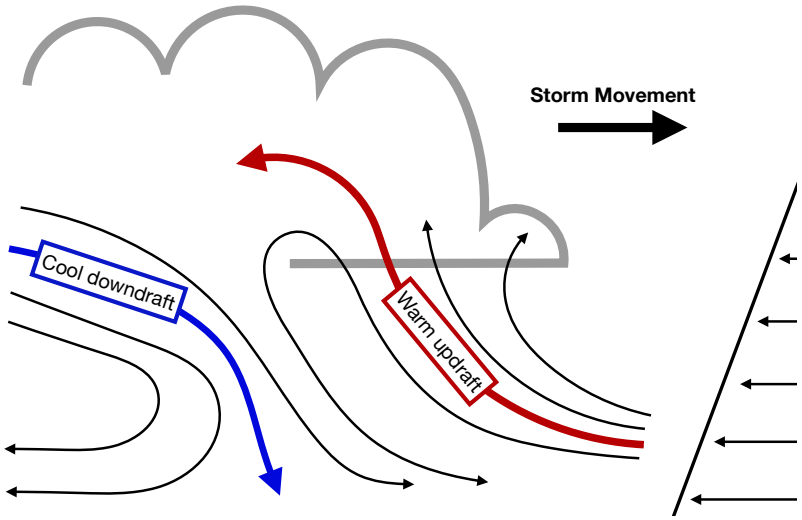

Figure 2.2: A schematic of a multicell storm environment in the presence of a low-level shear, with arrows representing streamlines of the flow.

Convection is found over many scales, from microscale turbulence to cloud-scale up and downdrafts to squall lines and hurricanes (Emanuel, 1994). This thesis focuses on convection within the mesoscale, which ranges in horizontal scale from about 2 km to 200 km, including thunderstorms, squall lines, and large downbursts. Convective storms can consist of varying numbers of convective cells. Single-cell storms consist of only one convective cell, or updraft-downdraft pair. These storms are short-lived and usually not strong enough to produce severe weather (Lin, 2007). However, a cluster of single-cell storms can exist within the same storm, creating a multicell storm, depicted in Figure 2.2. The existence of multiple cells and a moderate environmental shear can cause a multicell storm to form new cells along the gust front as old cells dissipate. Though the individual cells are short-lived, multicell storms can last several hours, especially in the presence of high vertical wind shear. Based on observations and simulations, the most severe and lengthy convective storms form and propagate in environments with high vertical wind shear. With the presence of a low-level shear such as that depicted in Figure 2.2, shear-induced circulation in front of the warm updraft can balance the cold outflow-induced circulation and produce deeper lifting of the warm updraft. In particular, conditions for a long lasting storm occur when the propagation speed of the region of cold air is approximate to the vertical wind shear (Lin, 2007). Along with shear, convective storms require strong

buoyancy to develop. It is sufficient to look at CAPE to determine the effect of buoyancy on the vertical velocity of the storm as the two measurements are directly related. If all of a parcel's CAPE is converted into kinetic energy, a theoretical maximum updraft velocity would be $(2 \cdot CAPE)^{1/2}$ (Lin, 2007).

Interactions between scales provide energy for the mesoscale to produce convective systems. For instance, mesoscale weather systems can be generated by temperature and vorticity advection associated with larger-scale flow systems such as fronts, as well as by energy transfer from smaller scales such as the organization of individual convective cells. Convective storms in the mesoscale are hard to predict numerically for a number of reasons: the uncertainty of the initial conditions derived from observations, the necessity of parameterizing small-scale effects such as turbulent mixing and microphysics, the variety of different scales interacting and exchanging energy with the mesoscale, and small-scale uncertainties will propagate to become errors in the mesoscale before reaching larger scales. Even if the CAPE of a parcel is known, it is difficult to determine if and when mechanical forcing will drive the parcel high enough to undergo convection (Lin, 2007).

2.2 Mathematical Background

The movement of all fluids can be described by a set of nonlinear partial differential equations: the Navier-Stokes equations. These equations can be described by the *continuity equation* for conservation of mass, the *momentum equation* for conservation of momentum, the *energy equation* for evolution of temperature, and an *equation of state* relating temperature and pressure, following Kundu and Cohen (2010) and Lin (2007). These equations are thus used to describe the movement of the atmosphere. In addition, the probability density function of surface wind speeds can often be described by a *Weibull distribution* (Weibull, 1951). The Weibull distribution will be used to compare wind speed observations and simulated wind speeds. Both mathematical preliminaries are described in this section.

2.2.1 Euler Equations

The conservation of mass equation for fluid motion, also known as the *continuity equation*, expresses that mass cannot be created nor destroyed. For a material volume, a volume occupied by a fixed set of fluid particles, mass must be conserved. The continuity equation is given by

$$\frac{\partial \rho}{\partial t} + \nabla \cdot (\rho \vec{v}) = 0, \tag{2.6}$$

where ρ is the density of a fluid, $\vec{v} = (u, v, w)$ is the velocity of a fluid, and $\nabla = (\partial/\partial x, \partial/\partial y, \partial/\partial z)$ is the differential operator.

Similarly, momentum is also conserved within a material fluid volume. Balancing forces on the material volume gives the *momentum equation*:

$$\frac{\partial \vec{v}}{\partial t} + (\vec{v} \cdot \nabla)\vec{v} = -\frac{1}{\rho}\nabla p + \nu \nabla^2 \vec{v} + \frac{1}{3}\nu \nabla(\nabla \cdot \vec{u}) + \vec{F}, \tag{2.7}$$

where p is the pressure of the fluid, ν is the kinematic viscosity, and $\vec{F}$ are the external body forces acting on the fluid.

To simplify, it is observed that viscous forces at the scales of interest are negligible, so it can be assumed that the fluid is inviscid. This assumption results in the Euler Equations for momentum:

$$\frac{\partial \vec{v}}{\partial t} + (\vec{v} \cdot \nabla)\vec{v} = -\frac{1}{\rho}\nabla p + \vec{F}, \tag{2.8}$$

where the body forces contained within $\vec{F}$ consist of the forces due to gravity, earth's rotation, and turbulent mixing. It is worth noting that WRF uses eddy viscosity instead of molecular viscosity to parameterize mixing from small-scale turbulence.

The thermodynamic *energy equation* for conservation of energy is written to show the evolution of temperature as:

$$\frac{D\theta}{Dt} = \frac{\theta}{c_p T}\dot{q}, \tag{2.9}$$

where $\dot{q}$ is the diabatic heating rate per unit mass, θ is the potential temperature, and $D/Dt = \partial/\partial t + \vec{u} \cdot \nabla$ is the material derivative.

Finally, the equation of state, relating temperature and pressure, for this system can be written as:

$$\theta = T(\frac{p}{p_s})^{R/c_p}, \tag{2.10}$$

where p_s is the surface pressure and $R = 287\ J/(kg \cdot K)$ is the ideal gas constant for dry air.

These are the governing equations for fluid motion in the dry atmosphere. In section 2.4, these equations are built upon by introducing terrain-following hydrostatic-pressure coordinates, the effects of moisture, spherical map projections, and the inclusion of physical parameterizations. These equations are then used within the WRF model.

2.2.2 Weibull Distribution

A Weibull distribution is used to analyze observed and simulated wind speeds. It has been shown that the Weibull distribution is a good fit in representing the probability density function of observed wind speed data (Tuller and Brett, 1984). The Weibull distribution function is given by

$$F(v) = \left(\frac{k}{c}\right)\left(\frac{v}{c}\right)^{k-1} \exp\left[-\left(\frac{v}{c}\right)^{k}\right], \tag{2.11}$$

where $F(v)$ is the probability of a wind speed v (m/s) occurring within the dataset, k the Weibull shape parameter (dimensionless), and c the Weibull scale parameter (m/s). Scale parameter c is proportional to the mean wind speed, whereas shape parameter k determines how wide the distribution is: a smaller k causes a wider spread of wind speeds about the mean (Stull and Ahrens, 2000).

2.3 Observational Data

Observations from both ECCC and NOAA are used to obtain information about atmospheric conditions from stations listed in Table 2.1. Sustained wind speed, wind direction, and temperature data are obtained from ECCC, while both sustained wind speed and gust speed are obtained from NOAA. These observations are used to assess the climatology of the region and to analyze the storm of interest. In addition, radar reflectivity data is obtained from NOAA to track the storm's path through the Great Lakes. Sea level pressure and relative humidity are extracted from reanalysis data obtained from NARR. These variables are used to analyze the atmospheric conditions of the pre-storm environment. NARR data is also used to initialize the WRF simulations.

Wind Data

Wind speed data was analysed using data provided by ECCC and NOAA from the stations outlined in Table 2.1. ECCC provides hourly sustained wind speeds as 2-minute averages for every hour. NOAA provides hourly sustained wind speeds as 1-minute averages for every hour, along with extra sub-hourly sustained winds recorded when a high-wind event occurs. In addition to sustained winds, the maximum wind gust speed during the sustained wind interval is recorded when the gust speed is high enough. These observations are used to determine the time, length, and approximate wind intensity of the storm of interest. Climatology is performed on ECCC's Erieau station and NOAA's Detroit station.

Table 2.1: The name and location of all ECCC and NOAA stations used to determine characteristics of the storm.

	Name	Type	Latitude	Longitude
Erieau	Erieau	ECCC	42.25	-81.90
A	South Bend International Airport	NOAA	41.71	-86.32
B	Capital Region International Airport	NOAA	42.78	-84.59
C	Toledo Express Airport	NOAA	41.59	-83.81
D	Detroit Metropolitan Wayne County Airport	NOAA	42.22	-83.35
E	Mansfield Lahm Regional Airport	NOAA	40.81	-82.52
F	Cleveland Hopkins International Airport	NOAA	41.41	-81.85
G	Erie International Airport	NOAA	42.08	-80.17

Due to the low temporal frequency of ECCC wind speed observations, along with the quick-moving and short-lived nature of summer storms, it is possible for the wind observations to miss a storm completely. Even if a storm is captured by wind speed observations, information about the intensity of the storm is lost due to the lack of gust speed observations. To remedy this, NOAA observations are used to supplement ECCC observations and estimate other features about the storm at ECCC stations.

Radar Data

NOAA reflectivity data is obtained from multiple Next-Generation Radar (NEXRAD) stations across the southern Great Lakes. These high resolution radar stations are operated by the National Weather Service of NOAA. The Integrated Data Viewer (IDV) Version 5.5 from UCAR/Unidata is used in the analysis and visualization of the data. A mosaic of station reflectivity outputs is created using the IDV to compare with simulated reflectivity outputs and to track the trajectory of the storm of interest. Radar stations send out radio waves into the atmosphere, and reflectivity is a measure of how much energy from a location is being reflected back to a radar station. Base reflectivity values are used to create plots, which is the reflected value from 0.5° elevation. At this level, precipitation is the main source of reflection, and thus the reflectivity shown on a map is indicative of rainfall. Reflectivity values of 20 dbZ corresponds to trace rain and reflectivity values of 60 dBZ correspond to intense rain rates of up to 100 mm/hour. Hail can form for values above around 53 dBZ (Stull and Ahrens, 2000).

Reanalysis Data

Reanalysis data provides snapshots of atmospheric conditions over long periods of time. Typically, observations from a variety of sources such as ground-based stations, ships, airplanes, and satellites are combined with forecasts from NWP models using data assimilation methods. The NWP forecast provides a first guess estimate for the conditions of the atmosphere, and observations are used to correct the forecast. Data for WRF simulations is provided by the North American Regional Reanalysis (NARR) model (Mesinger et al., 2006). The NARR model is a high-resolution climate dataset produced over a long term. Output from the NARR model is 8-times daily (ie. every 3 hours) with 0.3° resolution (or 32 km resolution at the lowest latitude) and 29 pressure levels. Variables are assimilated by the Regional Data Assimilation System (RDAS) and the high resolution National Centers for Environmental Prediction (NCEP) Eta Model (Mesinger et al., 2006). This data is outputted in Gridded Binary (GRiB) format. Sea level pressure and relative humidity are also extracted from NARR data. These variables are then horizontally interpolated and used to analyze the atmospheric conditions of the pre-storm environment. A description of this process can be found in Appendix A. While reanalysis data is partially based on observations, it is important to note that it is not entirely an observational data source and uncertainties may exist within the dataset (Parker, 2016).

2.4 WRF Model Summary

In addition to the wind climatology analysis, numerical simulations are performed using the WRF Advanced Research Model (version 4.0). WRF is a NWP model encompassing a variety of physics schemes, numerics options, and initialization routines. WRF uses the compressible, nonhydrostatic equations of motion with terrain-following coordinates, described in section 2.4.2 (Skamarock et al., 2008). Real-data simulations are performed by pre-processing data in GRiB format from the NARR model along with static geographical land data using the WRF preprocessing system (WPS). WRF is then initialized and forced at the boundaries with this data, discretized using a finite difference approach with fifth order (horizontal) and third order (vertical) advection with a time-split integration scheme. This section describes the properties of WRF, including the equations and parameterizations used in this thesis. A summary of simulations is also outlined.

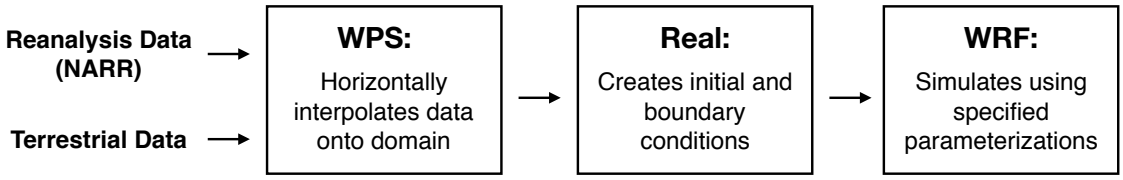

Figure 2.3: Summary of WRF processes to convert input data into a successful simulation.

2.4.1 WRF Model

The WRF model is used to perform all simulations outlined in this thesis. Initial and boundary conditions for the WRF model can either be defined manually for idealized simulations or defined using interpolated reanalysis data for real-data simulations. This thesis makes use of 3-hour meteorological reanalysis data provided by NARR to perform real-data simulations.

WPS is used to convert both geographical data and large-scale GRiB meteorological reanalysis data into an appropriate form necessary for WRF's real data processor. The program *geogrid* is run in order to define a physical grid with appropriate map projection, location, grid points, and grid distances. Similarly, the program *ungrib* is used to process appropriate fields from the GriB reanalysis data into an internal binary format. Finally, *metgrid* is run on the output from both of these programs: the meteorological data output from *ungrib* is horizontally interpolated onto the domain output from *geogrid*. Thus, a file is created for every three hours which contains real atmospheric values on an appropriate grid. These files contain three-dimensional atmospheric values of temperature, relative humidity, and horizontal momentum components and two-dimensional surface pressure, sea level pressure, soil temperature, soil moisture, snow depth, skin temperature, sea surface temperature, and sea ice. They also contain static terrestrial fields of albedo, Coriolis parameters, terrain elevation, vegetation, land/water mask, map scale and rotation factors, soil texture, annual mean temperature, and latitude/longitude. This data is then used by the program *real*, which processes the data into input for WRF. The *real* preprocessor vertically interpolates values from the free atmosphere to the model lid, and extrapolates if there are inconsistencies between the input surface pressure and WRF's surface pressure. Figure 2.3 summarizes the programs needed to initialize and run a WRF simulation using real data.

Spatial discretization in the WRF model is obtained using a C grid where velocities and thermodynamic variables are staggered a half grid-length away from each other. A

finite difference approach is used to discretize with a fifth order (horizontal) and third order (vertical) advection scheme. A time-split integration scheme is used, consisting of the following time integration schemes. Low-frequency modes are integrated using a third-order Runge-Kutta time integration scheme whereas high-frequency modes are integrated over smaller time-steps. Both gravity waves and horizontally propagating acoustic modes use a forward-backward time integration scheme, while vertically propagating acoustic modes use a vertically implicit scheme (Skamarock et al., 2008).

2.4.2 Model Equations

The governing equations used by WRF are the compressible, nonhydrostatic Euler equations with terrain-following vertical coordinates. This section will describe the formulation of these equations, following Skamarock et al. (2008). To reduce error in calculating the pressure gradient and buoyancy, the governing equations are solved in perturbation form, in which the variables are defined as perturbations from a reference state of hydrostatic balance.

Euler Equations with Terrain-Following Coordinates

Terrain-following hydrostatic-pressure vertical coordinates were first proposed by Laprise (1992) in order to naturally include a lower boundary condition which involves topography in nonhydrostatic models. The coordinate η is defined by

$$\eta = (p_h - p_{ht})/\mu, \tag{2.12}$$

where $\mu = p_{hs} - p_{ht}$ p_h is the mass per unit area of air in the column, p_h is the hydrostatic component of pressure, p_{hs} is the hydrostatic pressure of the surface boundary, and p_{ht} is the hydrostatic pressure of the top boundary. p_{hs} is a function of (x, y, t), while p_{ht} is a constant. η is defined to be 1 at the surface and 0 at the top boundary. A schematic of the coordinate system can be seen in Figure 2.4.

The flux-form variables used in WRF are defined as:

$$\mathbf{V} = \mu\mathbf{v} = (U, V, W), \tag{2.13}$$

$$\Omega = \mu\dot{\eta}, \tag{2.14}$$

$$\Theta = \mu\theta, \tag{2.15}$$

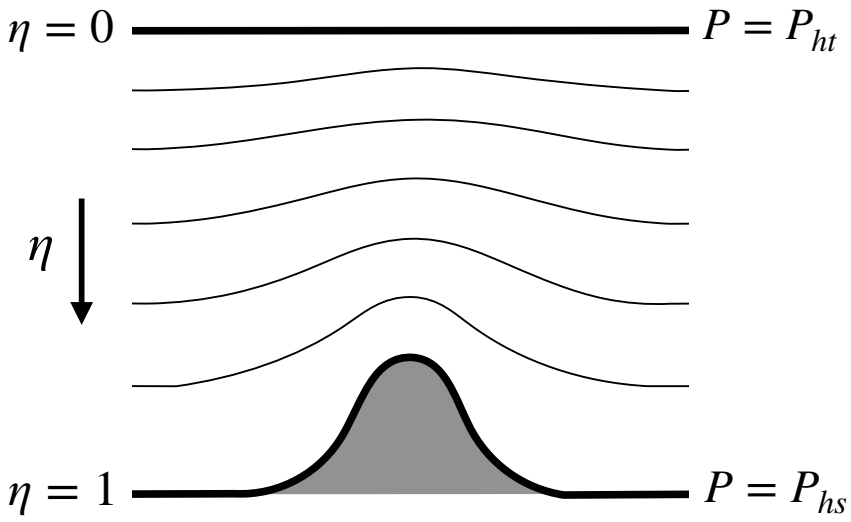

Figure 2.4: Schematic of the vertical eta-coordinates used in WRF.

where $\mathbf{v} = (u, v, w)$ is the covariant velocity, $\omega = \dot{\eta}$ is the contravariant vertical velocity, and θ is the potential temperature. The flux-form equations of motion for a dry atmosphere are written as

$$\partial_t U + (\nabla \cdot \mathbf{V}u) - \partial_x(p\phi_\eta) + \partial_\eta(p\phi_x) = F_U, \tag{2.16}$$
$$\partial_t V + (\nabla \cdot \mathbf{V}v) - \partial_y(p\phi_\eta) + \partial_\eta(p\phi_y) = F_V, \tag{2.17}$$
$$\partial_t W + (\nabla \cdot \mathbf{V}w) - g(\partial_\eta p - \mu) = F_W, \tag{2.18}$$
$$\partial_t \Theta + (\nabla \cdot \mathbf{V}\theta) = F_\Theta, \tag{2.19}$$
$$\partial_t \mu + (\nabla \cdot \mathbf{V}) = 0, \tag{2.20}$$
$$\partial_t \phi + \frac{1}{\mu}[(\mathbf{V} \cdot \nabla\phi) - gW] = 0, \tag{2.21}$$

with equation of state

$$p = p_0(R_d\theta\rho/p_0)^\gamma, \tag{2.22}$$

where $\partial_\eta\phi = -\mu/\rho$ is the diagnostic relation for hydrostatic balance, $\phi = gz$ is the geopotential, p the pressure given by the equation of state, p_0 a reference pressure, ρ the density, $\gamma = c_p/c_v = 1.4$ is the ratio of heat capacities for dry air, R_d the gas constant for dry air, and F_U, F_V, F_W, F_Θ are the forcing terms produced by parameterized physics, mixing, and the Coriolis effect.

Euler Equations with Moisture

Since atmospheric air is a mixture of dry air and water vapour, it is important to include moisture in the equations of motion. The vertical coordinate is now defined with respect to the dry atmosphere as

$$\eta = (p_{dh} - p_{dht})/\mu_d, \tag{2.23}$$

where μ_d is the mass per unit area of air in the column, p_{dh} is the hydrostatic pressure of the dry atmosphere, p_{dht} is the hydrostatic pressure at the top of the dry atmosphere. As such, the flux-form variables can be written with $\mu = \mu_d$:

$$\mathbf{V} = \mu_d \mathbf{v}, \tag{2.24}$$
$$\Omega = \mu_d \dot{\eta}, \tag{2.25}$$
$$\Theta = \mu_d \theta. \tag{2.26}$$

The moist Euler equations are then:

$$\partial_t U + (\nabla \cdot \mathbf{V}u) + \frac{\mu_d}{\rho}\partial_x p + \frac{\rho_d}{\rho}\partial_\eta p \partial_x \phi = F_U, \tag{2.27}$$
$$\partial_t V + (\nabla \cdot \mathbf{V}v) + \frac{\mu_d}{\rho}\partial_y p + \frac{\rho_d}{\rho}\partial_\eta p \partial_y \phi = F_V, \tag{2.28}$$
$$\partial_t W + (\nabla \cdot \mathbf{V}w) - g(\frac{\rho_d}{\rho}\partial_\eta p - \mu_d) = F_W, \tag{2.29}$$
$$\partial_t \Theta + (\nabla \cdot \mathbf{V}\theta) = F_\Theta, \tag{2.30}$$
$$\partial_t \mu_d + (\nabla \cdot \mathbf{V}) = 0, \tag{2.31}$$
$$\partial_t \phi + \frac{1}{\mu_d}[(\mathbf{V} \cdot \nabla\phi) - gW] = 0, \tag{2.32}$$
$$\partial_t Q_m + (\nabla \cdot \mathbf{V}q_m) = F_{Q_m}, \tag{2.33}$$

with new equation of state defined with respect to dry variables

$$p = p_0(R_d \theta_m \rho_d / p_0)^\gamma, \tag{2.34}$$

where $\partial_\eta \phi = -\mu_d/\rho_d$ is the diagnostic relation for hydrostatic balance, $\theta_m = \theta(1+q_v R_v/R_d)$ is the moist potential temperature, R_v is the gas constant for water vapour, and $Q_m = \mu_d q_m$ is the flux form of the mixing ratio for water species m, where m accounts for water vapour, clouds, rain, ice, etc. ρ_d is the density of dry air, whereas ρ takes into account the density of the entire parcel as $\rho = \rho_d(1 + q_v + q_c + q_r + q_i + ...)$ where the various q's describe the mixing ratio of water vapour, clouds, rain, ice, etc.

Table 2.2: Description of the simulations performed.

	Lake On	Lake Off	July 2 km	July 10 km
Start Time (UTC)	July 20 12:00	July 20 12:00	July 01 00:00	July 01 00:00
End Time (UTC)	July 23 00:00	July 23 00:00	July 31 21:00	July 31 21:00
Timestep (s)	6	6	3	15
Centre Latitude	44.97°N	44.97°N	43.55°N	43.5°N
Centre Longitude	86.53°W	86.53°W	86.53°W	85.25°W
Resolution	2 km	2 km	2 km	10 km
E/W Grid Points	1100	1100	1100	250
S/N Grid Points	950	950	800	180
Number of eta Levels	60	60	30	60
Lake Erie/Lake St. Clair Land Use	Inland Lake	Evergreen Broadleaf	Inland Lake	Inland Lake

2.5 Description of Simulations

Four simulations will be discussed in this thesis. Two storm-scale WRF simulations are performed at 2 km resolution to investigate this storm: a simulation with standard geographical data, referred to as Lake On, and one with Lake St. Clair and Lake Erie defined as land, referred to as Lake Off. The domain for these simulations is shown in Figure 2.5, with the inner box denoting the land area that has been altered in accordance with Section 2.5.2. To gain perspective on long-term summer wind speeds, an additional simulation with standard geography and a 2 km resolution is run for the entire month of July 1998, referred to as July 2 km. In interest of simulation time, this simulation is run with reduced north/south grid points and eta levels. This resolution is shown to be sufficient to represent the time, location, and structure of mesoscale convective storms more accurately than simulations with grids of 10 km and a convective parameterization (Done et al., 2004). To analyze this claim, an additional simulation is performed with 10 km grid spacing and a Kain-Fritsch cumulus parameterization. This simulation is run for the entire month of July 1998 in order to analyze the parameterization's effects on general wind speeds along with storm formation and propagation. It is referred to as July 10 km. Further details of simulation parameters are found in Table 2.2.

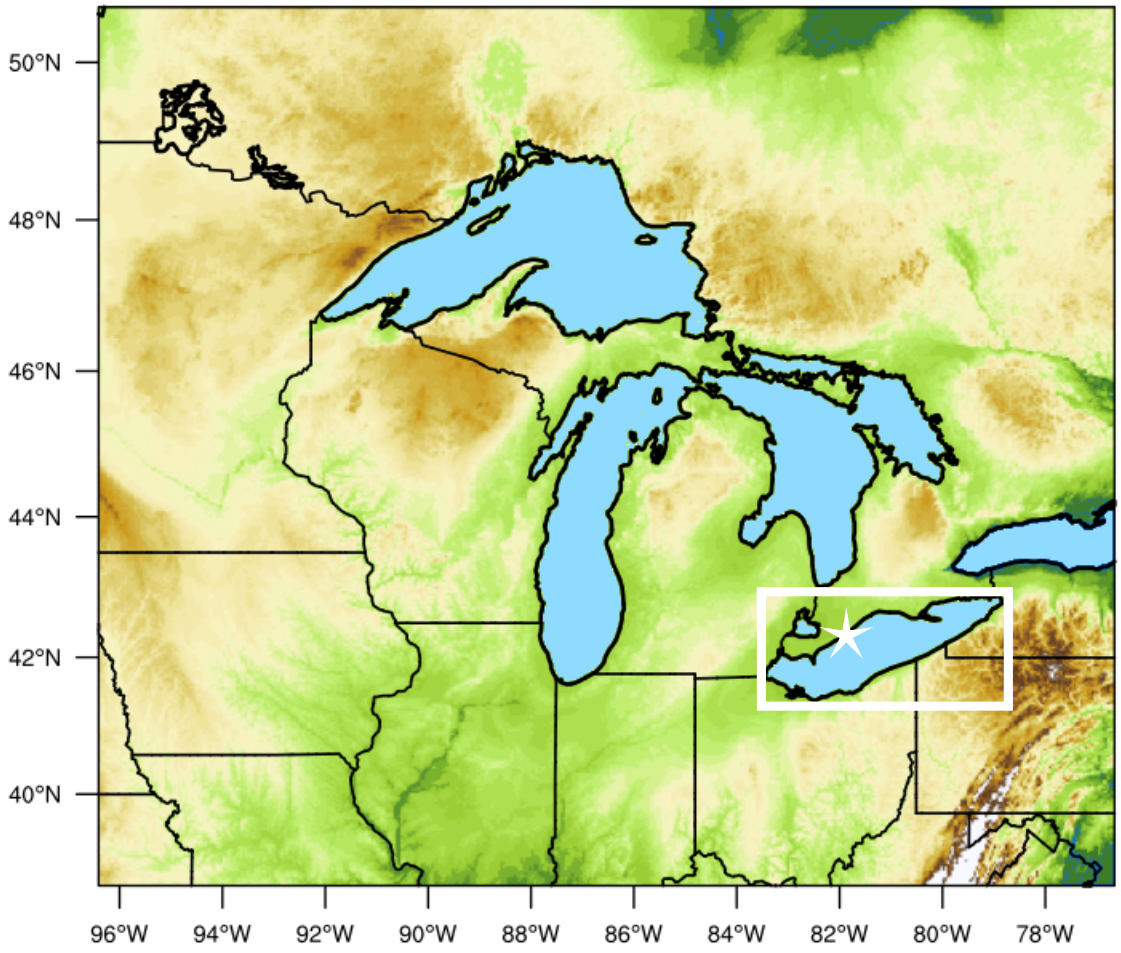

Figure 2.5: Domain of both the Lake On and Lake Off simulations. The inner box denotes the land area that has been altered, and the star denotes Rondeau Park.

2.5.1 Parameterizations

A list of parameterizations used in the simulations can be found in Table 2.3. A description of each parameterization is given following Skamarock et al. (2008). It is noted that cumulus parameterization is chosen to be off for many of the simulations due to the fine grid resolution. The surface layer, land-surface, and boundary layer schemes are called at every timestep, whereas the radiation, cumulus, and microphysics schemes do not need to

Table 2.3: Parameterizations and options used in the simulations.

Parameterization Type	Parameterization Scheme
Cumulus Physics	Kain-Fritsch (10 km resolution only)
Microphysics	WRF Single-moment 3-class
Radiation Physics	Dudhia Shortwave and RRTM Longwave
Land Surface Physics	Unified Noah Land Surface Model
Surface Layer Physics	MM5 Similarity Scheme
Planetary Boundary Layer	Yonsei University Scheme
Turbulence Option	Diffusion evaluated on eta surfaces
Eddy Viscosity Coefficient	Horizontal Smagorinsky first order closure

be called (and are often too expensive to be called) every timestep. Figure 2.6 shows how each of the parameterizations interact with each other.

Cumulus parameterization is necessary for large grid spacing where convection is not resolved. Since cumulus parameterization assumes that convective cells are entirely sub-grid scale and that grid cells contain many convective cells, they are valid only for coarse grids (with grid spacing greater than or equal to 10 km). At this coarse grid scale, latent heat can be released in the convective columns at a proper time-scale. In the 5-10 km grid resolution range, these schemes have often been found to be helpful in triggering convection, although the assumptions about sub-grid scale convective cells will not hold (Skamarock et al., 2008). Most simulations in this thesis have a finer grid resolution than 5 km, so cumulus parameterization is not used for those. A Kain-Fritsch (Kain, 2004) scheme is used for a simulation with 10 km grid resolution. This mass flux scheme uses a simple cloud model with moist updrafts and downdrafts which includes detrainment, entrainment, and simple microphysics, as outlined in Figure 2.7.

Microphysics parameterizations act to resolve processes involving water vapour, clouds, and precipitation. A WRF Single-moment 3-class microphysics is used, following Hong et al. (2004), with computational features outlined in Hong and Lim (2006). Although summer simulations are run, this microphysics scheme includes a simple-ice scheme, meaning that it predicts vapour, cloud water/ice, and rain/snow. For temperatures above freezing, such as those in the simulations run in this thesis, cloud water and rain are assumed. Mixed-phase processes are not needed, and thus not included in this parameterization.

Surface layer schemes create friction velocities and exchange coefficients necessary for surface flux calculations in the land surface model and planetary boundary schemes. Simulations use the MM5 Similarity Scheme as a surface layer scheme, which considers stability functions from Paulson (1970), Dyer and Hicks (1970), and Webb (1970) to compute heat,

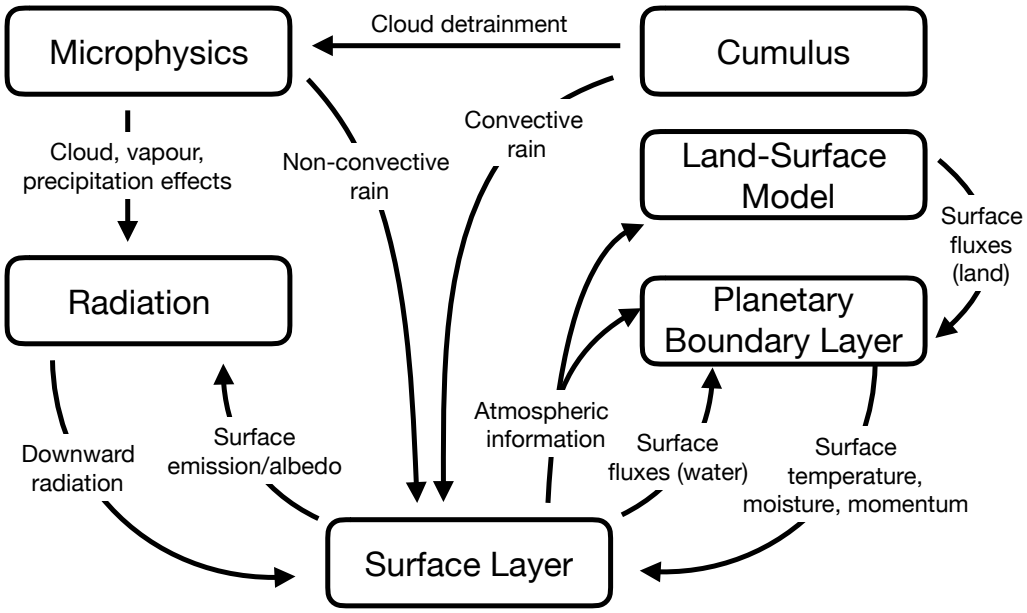

Figure 2.6: Schematic demonstrating how each of the parameterizations interact with each other, modified from Dudhia (2014) to include interactions with the Land-Surface Model.

moisture, and momentum surface exchange coefficients.

Land-surface models calculate heat and moisture fluxes over land, which are then passed to the boundary layer scheme. To calculate the surface fluxes, it uses land data along with atmospheric information from the surface layer scheme, radiative forcing from the radiation scheme, and precipitation forcing from the microphysics and convective scheme. The heat and moisture fluxes are used as a lower boundary condition in which the planetary boundary layer scheme calculates vertical transport. The 4-layer soil temperature and moisture model, the Noah scheme, is used in each simulation. The model can predict both canopy moisture and snow cover, and takes into account the root zone, evapotranspiration, soil drainage, runoff, vegetation categories and fraction, and soil texture.

The planetary boundary layer calculates sub-grid scale vertical fluxes due to eddy transports. These fluxes occur in the entire atmospheric column, thus are not limited to the boundary layer. The planetary boundary layer scheme determines the flux profiles for temperature, moisture, and horizontal momentum in the well-mixed boundary layer and the stable layer. The Yonsei University scheme is used for each simulation presented in this paper (Hong et al., 2006). The height of the boundary layer is determined from the

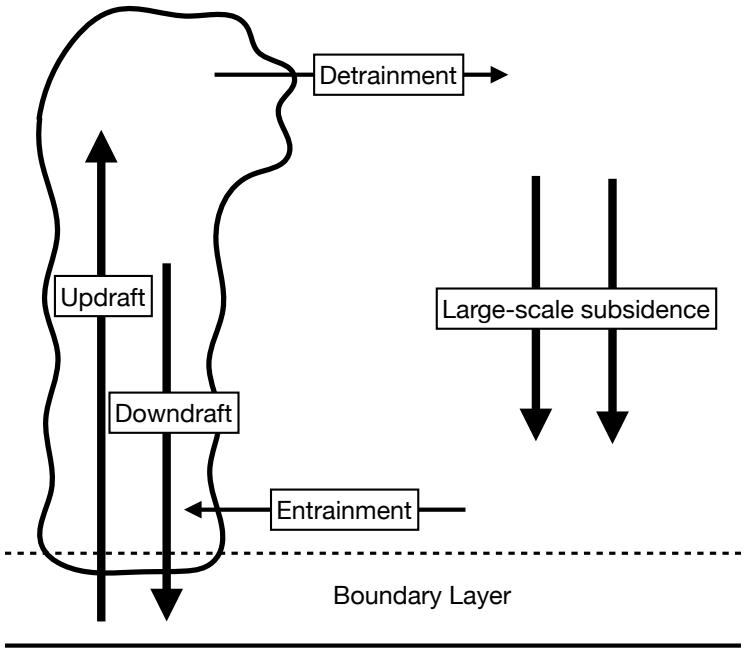

Figure 2.7: Schematic demonstrating the processes taking place in the Kain-Fritsch cumulus parameterization scheme.

buoyancy profile, with enhanced vertical coefficients in this region. A counter-gradient flux for heat and moisture is employed in unstable conditions. Horizontal mixing is performed separately with a horizontal Smagorinsky eddy viscosity on eta surfaces.

The atmospheric radiation schemes consider radiative flux divergence and downward radiation at the surface in order to provide appropriate atmospheric heating. Both longwave radiation (infrared and thermal radiation absorbed and emitted by gases and surfaces) and shortwave radiation (visible and near-visible wavelengths from the solar spectrum) schemes are used. Radiation differences are caused by clouds and water in the atmosphere, carbon dioxide, ozone, and trace gases. The radiation schemes are one-dimensional column schemes with each column treated independently of the others. Since the fluxes correspond to those in an infinite horizontal plane, these schemes are good approximations if the vertical grid spacing is much less than the horizontal grid spacing. In the finest horizontal resolution simulations in this thesis, the horizontal spacing is nearly 20 times larger than the vertical spacing, and thus the approximation holds. For longwave radiation, the Rapid Radiative Transfer Model is used (Mlawer et al., 1997). This model is a spectra-band scheme using the correlated-k method. Longwave processes due to water vapour, ozone,

carbon dioxide, and gases are represented in pre-set tables. The Dudhia (Dudhia, 1989) model is used for shortwave radiation processes. The solar flux is downward-integrated accounting for clear-air scattering, water vapour absorption, and cloud albedo and absorption. Clouds are represented in tables defined by Stephens (1978).

2.5.2 Altering Land Data

In order to assess the effects of Lake Erie and Lake St. Clair on the storm, a simulation is performed in which both lakes are defined as forests. Such sensitivity testing can be performed by modifying the data output by *geogrid* before *metgrid* is run. Details of this process can be found in Appendix A. To ensure the surface inputs are not overwritten when *real* is run, the surface input source is set to not overwrite the soil categories that are given from *geogrid*.

For this simulation, a 214 x 524 km rectangle surrounding both Lake Erie and Lake St. Clair, shown in Figure 2.5, is altered with a number of changes to geographical variables. The land mask is changed from water to land and the land-use index is set to a Deciduous Broadleaf Forest according to the USGS 24-category system. The lake depth is set to default values for land. The soil temperature was changed to 280°K and the bottom and top (dominant and non-dominant) soil categories are changed to neighbouring values. Similarly, the fraction of each land cover type is changed to the value of surrounding land cover.

Chapter 3

Observational Data Analysis

Many different sources of observational data (outlined in Section 2.3) are used in this thesis. Wind speed and gust speed data obtained from ECCC and NOAA are used to perform a climatology of high-wind events over a twenty year observation period. This data is used to determine typical lengths and intensities of different high wind events throughout the year. In addition, NOAA's wind gust data is used to determine typical gust strengths for given sustained wind speeds. Reanalysis data from NARR and reflectivity data are used along with the wind data to determine characteristics about the storm in question: the large scale atmospheric conditions present during the formation of the storm, how the storm propagates, and how strong the winds were recorded to be in various locations along the path of the storm.

3.1 Climatology

In order to determine how typical the July 1998 winds are in the region, climatology was performed on ECCC's Erieau and NOAA's Detroit wind speed data. Both locations are at roughly the same latitude and approximately 120 km apart. Detroit is on the west side of Lake Erie, inland between Lake Erie and Lake St. Clair, while Erieau is directly on the water on the northern shore of Lake Erie. According to previous climatologies (Bentley and Mote, 1998; Johns and Hirt, 1987; Schoen and Ashley, 2011), both stations see a frequent level of summer storms: usually the same storm will pass over both locations. Climatologies from both locations are compared and discussed, with wind speed data analyzed in order to approximate wind gusts at Erieau.

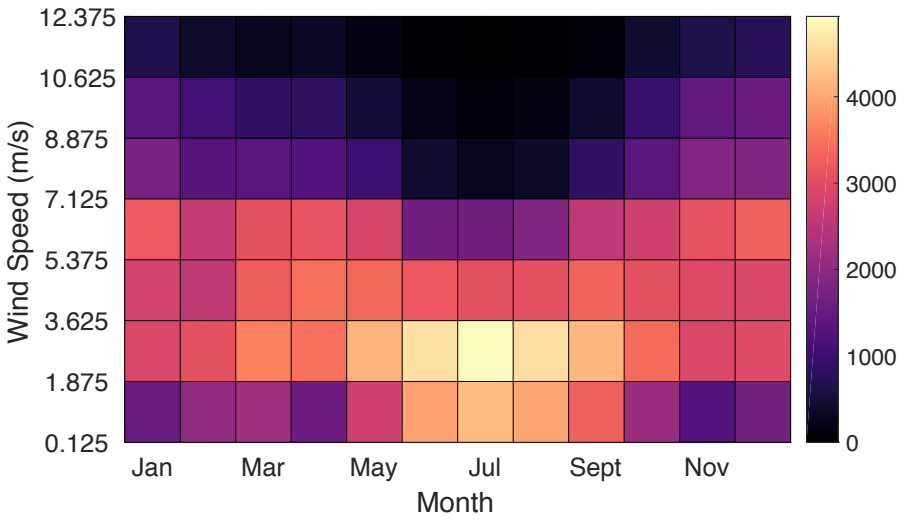

Figure 3.1: Total number of observations with a given wind speed in each month. Data is from the Erieau Station from 1995-2015, using hourly 2-minute averages.

3.1.1 Erieau Climatology

Climatology was performed for ECCC wind speed data collected at the Erieau station between 1995 and 2015. Figure 3.1 shows the total number of observations with a given wind speed each month. The winter months of November-February see the broadest range of wind speeds, with the highest wind speeds reaching over 12 m/s. During these winter months, there is a 24% chance that a single wind observation has speeds greater than 7.5 m/s, and only a 5.9% chance of wind speeds less than 1.5 m/s. Alternatively, the summer months of June, July, and August often have lower wind speeds, over half of which are in the 0-3 m/s range: a single wind observation has a 17% chance of wind speeds less than 1.5 m/s and a 35% chance of wind speeds between 1.5 m/s and 3 m/s. There is only a 2.8% chance of an observed summer wind observation with speeds greater than 7.5 m/s. Winter and summer winds vary greatly in range and intensity, with the range of winter wind speeds doubling the summer range. Because of this, a 10 m/s wind event in the summer is much more unlikely than a 10 m/s event in the winter.

To explore the length of wind events throughout the year, Figure 3.2 shows the number of events that are observed to be higher than a threshold wind speed for different lengths of time. The likelihood that there will be a summer wind event with a high sustained wind

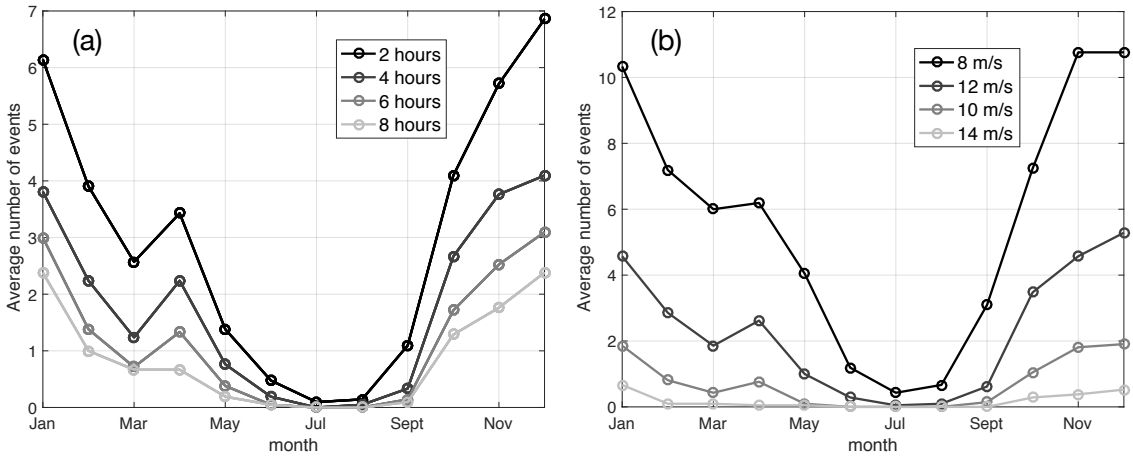

Figure 3.2: Average number of sustained wind events with (a) varied minimum lengths that have wind speeds less than or equal to 10 m/s, and (b) varied minimum wind speeds that last at least 3 hours. Data was taken at the Erieau Station from 1995-2015, using hourly 2-minute averages.

speed for multiple hours is extremely low. An event with 8.5 m/s sustained winds for 3 consecutive hours happens in only 33% of Julys. An event with a sustained wind speed of 10 m/s or higher for 2 or more consecutive hours in July has only happened once in twenty years of data. When summer wind events do last multiple hours, there is a much lower sustained wind speed than in winter months. This period of low wind speed and shorter sustained wind event length is due to the convective and short-lived nature of summer storms; storms are typically generated by frontal systems or in late afternoon after diurnal surface heating and can last anywhere from 30 minutes in the case of a single cell storm to over 6 hours in the case of a mesoscale convective complex (Maddox, 1980). Winter wind events in November, December, January, and February are strong and last longer. For instance, it is common to see about 3 events per month with 10 m/s sustained winds for at least 6 hours in the winter months.

3.1.2 Detroit Climatology

Similar climatology analysis was performed for NOAA's Detroit station in addition to ECCC's Erieau station. This station is located on the west side of Lake St. Clair, far

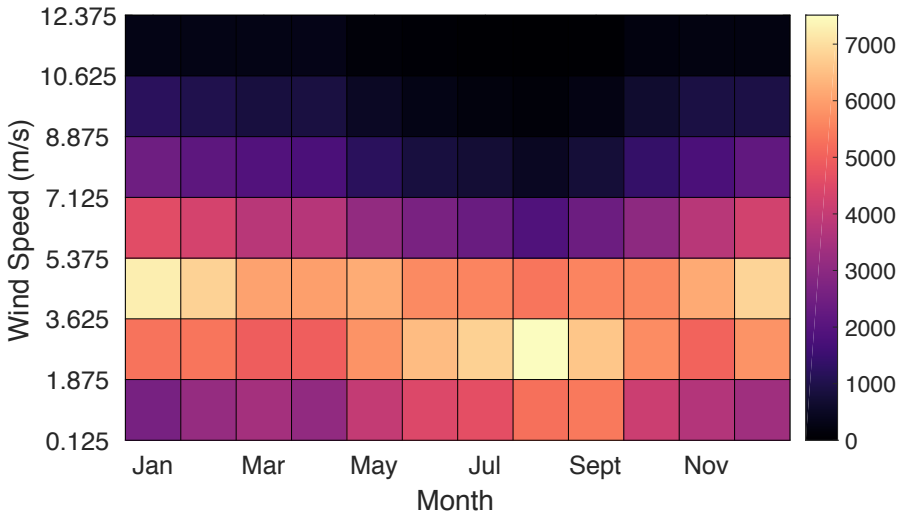

Figure 3.3: Total number of observation with given wind speed in each month. Data is from the Detroit Station from 1995-2014, using hourly 1-minute averages along with sub-hourly sustained wind observations.

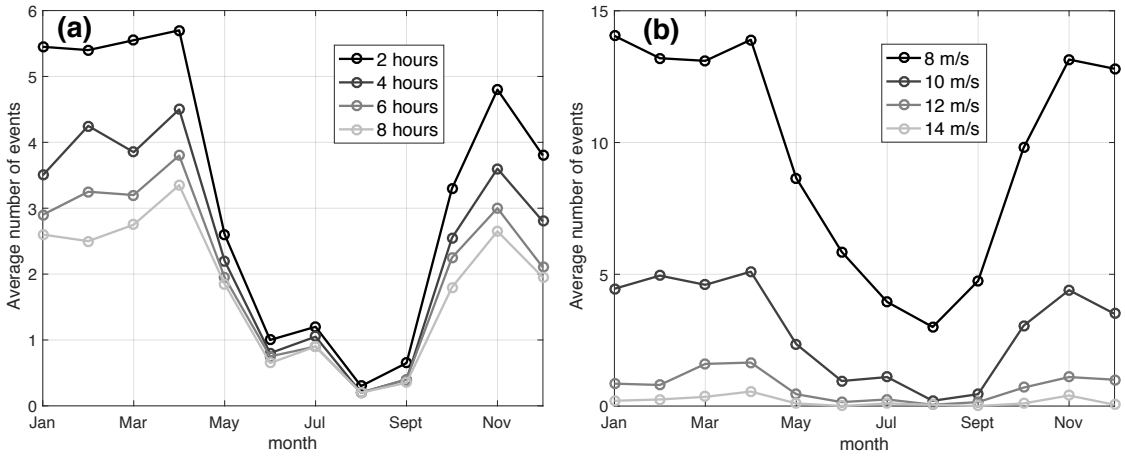

Figure 3.4: Average number of sustained wind events with (a) varied minimum lengths that have wind speeds less than or equal to 10 m/s, and (b) varied minimum wind speeds that last at least 3 hours. Data is from the Detroit Station from 1995-2014, using hourly 1-minute averages along with sub-hourly sustained wind observations.

Table 3.1: Sustained wind speed and gust speed observations for Detroit.

Time (UTC)	Wind speed (m/s)	Wind gust (m/s)
July 21 22:01	7.6	N/A
July 21 22:18	14.7	21.9
July 21 22:26	20.6	29.5
July 21 22:54	6.7	9.8
July 21 23:01	5.8	9.4

enough inland to ignore effects from the lake. The station is also located at an airport, presumably surrounded by buildings, tarmac, and a lack of surface vegetation. Figure 3.3 shows the total number of observations with any given wind speed and Figure 3.4 shows a sustained event analysis for Detroit. It is important to consider that NOAA observations include sub-hourly wind speed observations during higher-wind events. As hourly wind observations are not always associated with an hourly timestamp, sub-hourly observations were not removed from the data set for this comparison. This affects Figure 3.3 such that it will include these higher wind speeds, and Figure 3.4 in that a sub-hourly observation may determine if a wind event is not included in the total sustained events.

Erieau and Detroit differ in the percentage of observations per month that fall into various wind speeds in a number of ways: the months with the lowest wind speeds in Detroit are August and September, while the month with the lowest wind speeds in Erieau is July. In the summer months, Erieau will seldom experience wind speeds greater than 7.1 m/s, while Detroit manages to host a small fraction, which could be a result of the sub-hourly wind observations. In the winter, Detroit also will see more wind speeds in the lowest range of 0.1 m/s to 1.9 m/s. This could be due to the topograpy: Detroit is inland, while Erieau is near water. Overall, the number of sustained summer events is higher in Detroit than it is in Erieau. While the winter months of November-February appear to act similarly in Erieau, the winter months in Detroit tend to continue into March and April in Detroit, with April hosting the most sustained wind events out of any month. In the summer months, July has the most sustained events of 10 m/s or over for any length of time, as opposed to June, August, and even September, which acts as a summer month in Detroit.

As observed in Detroit, effects of the storm in question last for only one hour of strong winds, as outlined in Table 3.1. An event such as this would not appear in Figure 3.4: although the winds are extremely strong, the storm passes over the area very quickly.

Wind Gust Analysis

Due to the lack of information on wind gust strength for ECCC's Erieau station, wind gust analysis was performed for a nearby NOAA station in Detroit. When a high-wind event occurs, NOAA collects multiple wind observations throughout the storm in addition to hourly observations. Wind gusts are recorded as the maximum 3 second gust over a 1 minute period, rather than the 1-minute average of sustained wind. Twenty years of summer data recorded between 1995 and 2014 from the months of June, July, and August were analyzed. Gusts appear to only be recorded if their speed is higher than 7 m/s and at least 1.25 m/s higher than the sustained wind. Figure 3.5 shows a scatter plot of the sustained wind speed and associated gust speed for twenty years of data from the Detroit station. From this, information relating observed winds to gust strength can be determined. The gusts can consistently be approximated as about 2-8 m/s higher than their sustained values, with the mean gust speed of 3.67 m/s higher or 144% higher than the sustained speed. The highest gust recorded is 21 m/s faster than the associated sustained wind speed. The average sustained wind speed that has an associated wind gust is 7.7 m/s, whereas the average wind gust is 11.4 m/s. The most-occurring sustained-gust combination is a sustained speed of 7.1 m/s and a gust of 10.3 m/s.

3.2 Storm Characteristics

To determine the large-scale atmospheric features that could contribute to storm formation, reanalysis sea level pressure and relative humidity data from NARR are shown for North America in Figure 3.6 for before and during the storm. Skin temperature over the Great Lakes is shown in Figure 3.7 as the storm is forming. A strong low-pressure system passes eastward to the north of the Great Lakes on July 21 1998. There is a strong temperature and humidity gradient associated with a cold front to the south of the low pressure zone. Large-scale geostrophic winds are oriented from the north-west over the great lakes in line with the radar-observed storm path shown in Figure 3.8. The convective activity seems to be associated with a squall line forming along the cold front. This is in line with descriptions of a midlatitude synoptic-scale situation favourable for severe thunderstorm development (Johns and Doswell, 1992).

Using radar reflectivity data and wind speed data from stations across Ontario and the northern United States, more specific information about the storm is obtained. NOAA radar data shows that a strong convective storm formed on July 21, 1998 at 19:00 UTC around 42°N and 90°W. It moved east towards Lake Erie at an estimated rate of around

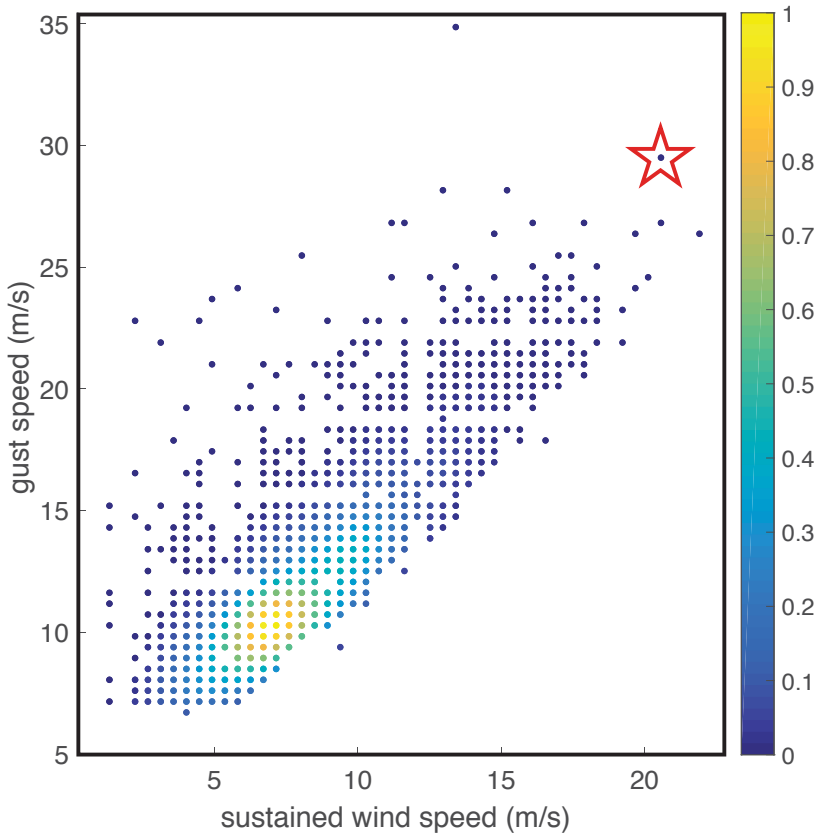

Figure 3.5: A scatter plot of the sustained wind speeds and their associated gust speed coloured by density. Data was taken from the Detroit Station from 1995-2014 at every time in which a gust observation is present. The star denotes the observation on July 21 22:26 UTC when the storm of interest is present in Detroit.

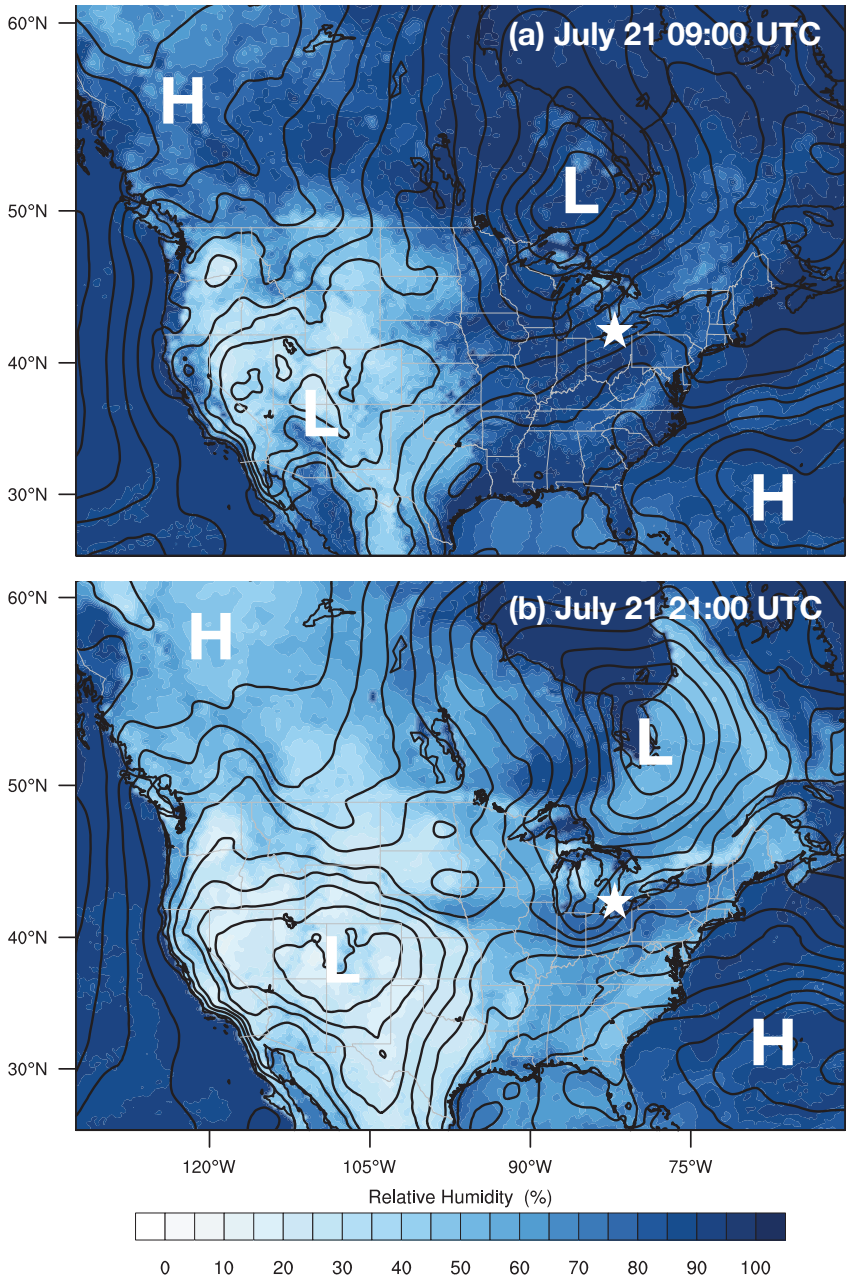

Figure 3.6: Relative humidity (%) with sea level pressure contours for produced with NARR data for (a) July 21 09:00 UTC, the morning before the storm, and (b) July 21 21:00 UTC, as the storm is propagating towards Lake Erie. H denotes a high pressure zone, L denotes a low pressure zone, and the star denotes Rondeau Park.

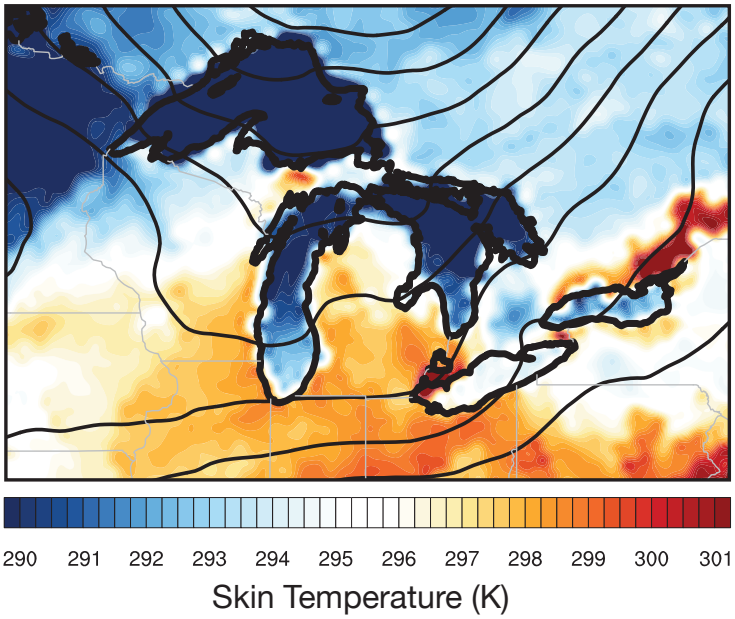

Figure 3.7: Skin temperature (K) with sea level pressure contours produced with NARR data for July 21 12:00 UTC, as the storm is forming.

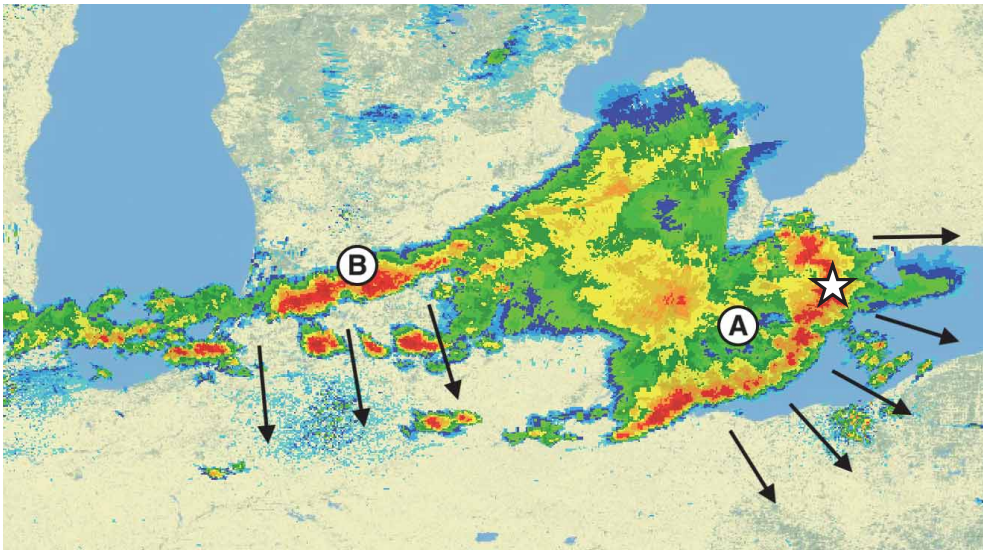

Figure 3.8: Radar reflectivity images provided by NOAA showing Peak A and Peak B of the storm at June 21 23:30 UTC, with arrows depicting the direction of storm movement. Rondeau Park is denoted with a star.

100 km/h. Figure 3.8 shows the radar reflectivity as the storm begins to pass over Lake Erie. The main bulk of the storm continued to propagate for 10 hours and traveled 1000 km before eventually dissipating in Pennsylvania. Observations from NOAA stations listed in Table 3.2 are used to determine, as the storm front passes by, that a sustained wind speed of the gust front is consistently around 12.5 m/s with gusts of up to 30 m/s, shown in Figure 3.9, which is discussed in more detail below.

As discussed above, NOAA collects multiple wind observations throughout the storm, whereas recordings for ECCC are only recorded hourly. Due to the nature of these observations, data for ECCC's Erieau station could potentially miss the storm completely. Analysis was performed on NOAA data in order to help fill in the gaps within the ECCC data at Erieau. Multiple locations listed in Table 2.1 along the path of the storm were considered. Using radar data, the approximate time of the storm passing each station was recorded. For each station, the first high-wind observation (with gusts of over 15 m/s) that occurred within the approximate time of the storm was used to determine the beginning of the storm front passing. The observations following the first gust were added to the series until the gust speed dropped below 15 m/s or until the gusts were no longer recorded.

Based on this data, it appears that two distinct peak wind events (Peak A and Peak B)

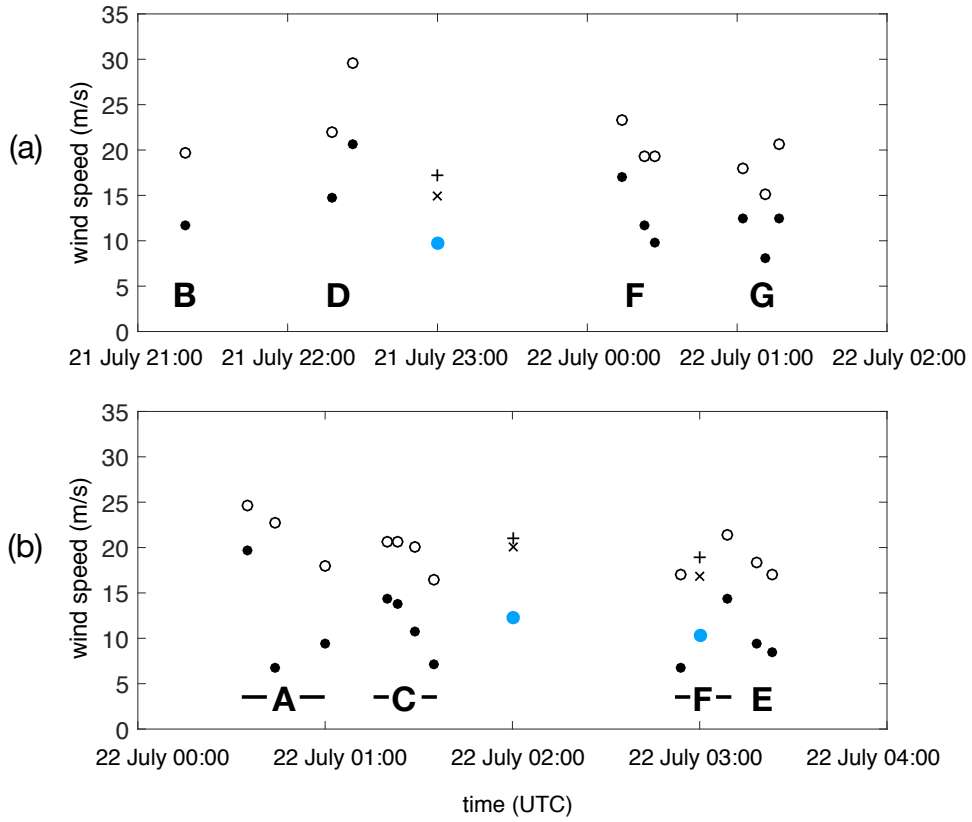

Figure 3.9: Observed wind speeds of (a) Peak A and (b) Peak B storm fronts at several locations as the storm traverses near Lake Erie. Closed black circles denote observed sustained wind speed at NOAA stations, closed blue circles denote observed sustained wind speed at Erieau, open circles denote observed gust speed, '+' denotes estimated gust speed at Erieau based on average difference in wind speed from gusts to sustained speed, and 'x' denotes estimated gust speed at Erieau based on the average percent of gust speed above sustained wind speed. The letters A through G denote the station that provided the observation, as listed in Table 2.1.

within the storm had traversed through the Lake Erie area. Referencing radar reflectivity data from NOAA shown in Figure 3.8, the main storm (Peak A) passes eastward though stations B, D, Erieau, F, and G. As the storm is dissipating, another clear band of high reflectivity is formed in a horizontal band and moves southward though stations A, C, F, and E. While only Peak A passes through Erieau, the effects of Peak B seemed to lengthen the effects of the storm. Wind speed and gust data from each of these stations was analyzed as a time series for each peak wind event in Figure 3.9. Detailed observations by NOAA stations record the maximum gust strength in the approximate 15 minute interval after the storm front hits to be about 8 m/s faster, or about 160% higher than sustained winds. This is much higher than the average difference discussed in section 3.1, providing evidence that the gusts of this storm are more powerful than average summer storms. Since the ECCC data only contains a 2-minute average wind speed and not a peak gust speed, the 160% gust strength at the NOAA station can be used to estimate the approximate gust speeds at the Erieau station. Sustained wind speeds, gust speeds, and estimated gust speeds are shown in Figure 3.9. This shows that the wind speed remained high along the gust front for both events for multiple hours. The wind speeds and estimated gusts at Erieau were not larger than at other locations the storm hit. However, due to the uncertainty of whether or not the wind observations at Erieau occurred during the storm front, more detailed simulations were performed (see section 4).

Wind observations from ECCC's Erieau station, which are given in Table 3.2 contain low temporal resolution, lack of gust information, and missing data. As a result, observations may have missed the gust front completely. The missing data could be a result of a broken wind gauge, claimed to have broken during a 50 m/s wind gust (Larson and Waldron, 2000). Sustained winds from Peak A and the effects of Peak B occur over a 5-6 hour range, but are only defined by three non-missing observation points. Sustained wind speeds like this are not completely out of the ordinary, but are quite rare during the summer months, with an average of 0.2 events in July with 2 hours of 10 m/s sustained wind, as shown in Figure 3.2.

Wind observations from NOAA's Detroit station provide more information on the storm peak as it begins to pass over Lake Erie. Due to the temporal frequency of observations, it can be stated that the storm peaks over Detroit on July 21 between 22:18 and 22:54 UTC, with the peak observation occurring at 22:26 UTC. This observation is denoted in Figure 3.5 as a star, showing that the sustained wind speed observation of 20.6 m/s is the second highest recording of sustained wind speed and the gust speed of 29.5 m/s is the second highest recording of gust speed in the twenty years of observations at this station. This is indicative of extremely powerful winds, in terms of both the sustained speed and high wind gusts. To put this into perspective, the highest gust speed recorded has a much

Table 3.2: Sustained wind speed observations for the Erieau station.

Time (UTC)	Wind speed (m/s)
July 21 23:00	10
July 22 00:00	4
July 22 01:00	1
July 22 02:00	12
July 22 03:00	10
July 22 04:00	Missing
July 22 05:00	7

lower sustained speed than this observation, while the highest sustained speed recorded has a significantly lower gust speed.

Chapter 4

Simulation Results

To gain a better perspective of the dynamics within the storm, three simulations with 2 km grid resolution are performed: one for the month of July 1998, and two storm-scale simulations for 60 hours leading up to and after the storm with both realistic topography and with Lake St. Clair and Lake Erie replaced by land variables instead of lake variables. To assess the need for the computationally-heavy fine resolution, a similar simulation is run for the month of July 1998 with 10 km grid resolution and a convective parameterization. Details of all simulations are listed in Table 2.2 and model parameterizations are listed in Table 2.3.

4.1 High Resolution Simulations

Two simulations are analyzed in this section: the 2 km resolution simulation performed for the length of the storm, and a similar simulation with 2 km resolution run for the month of July 1998. The month-long simulation differs in the zonal extent of the domain and number of eta levels in order to reduce the computational cost of the simulation. Both the simulated wind speeds over the month of July as well as storm-specific atmospheric characteristics of these simulations are compared to observations from ECCC and NOAA. The storm-scale simulation is then used to define significant characteristics of the storm as well as its propagation and effects.

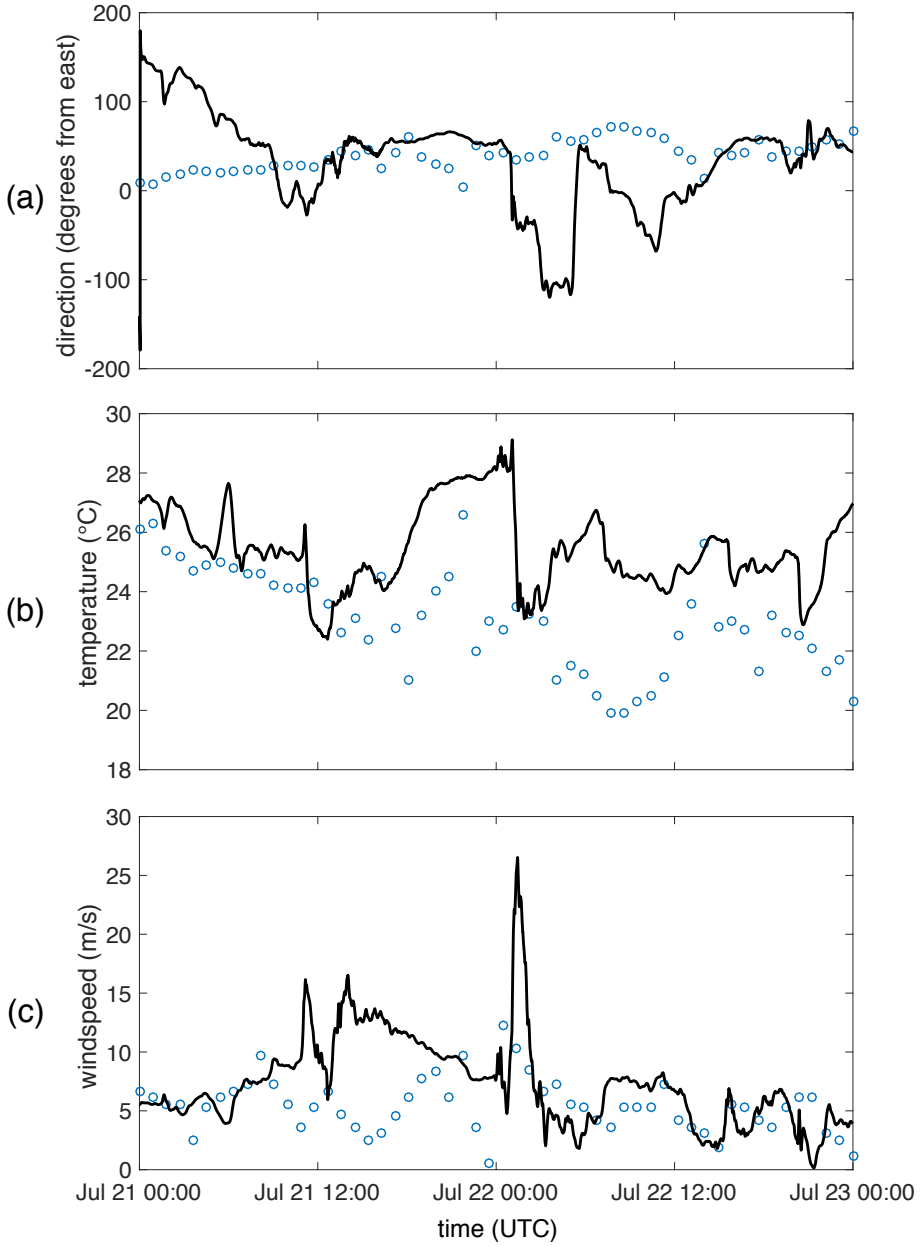

Figure 4.1: Direct comparison of observed (blue circles) and simulated (black line) (a) direction, (b) temperature, and (c) wind speed from the perspective of Erieau.

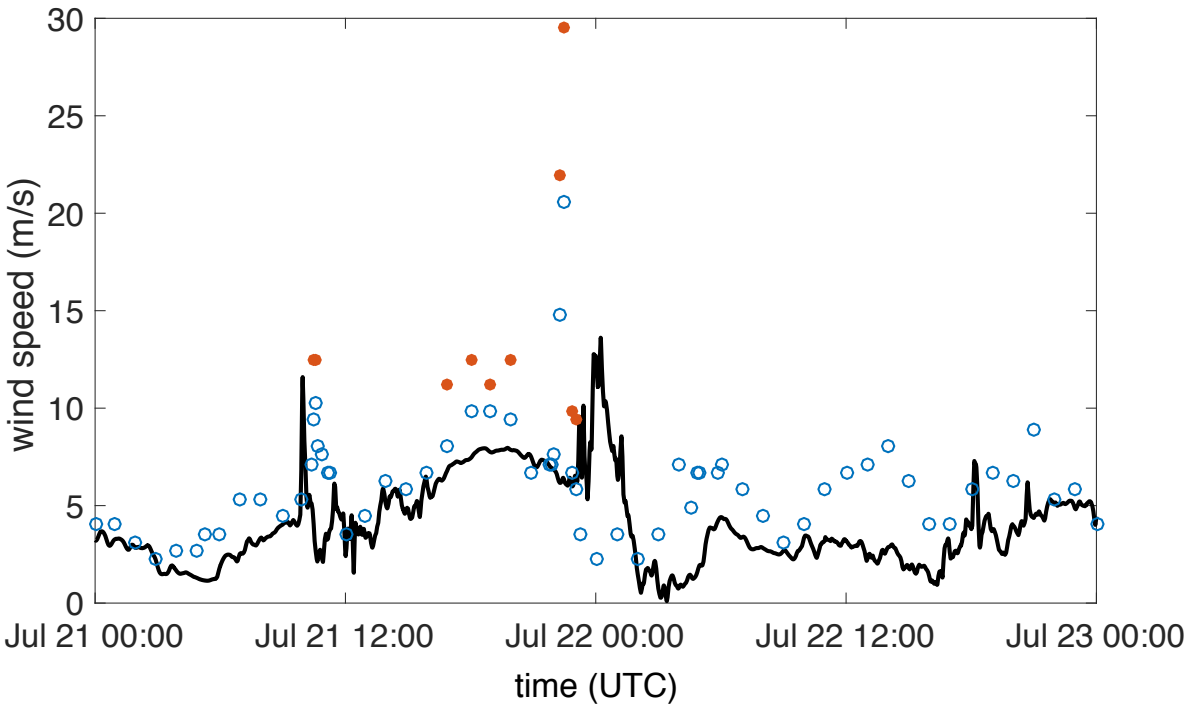

Figure 4.2: Direct comparison of observed sustained wind speed (open blue circles), wind gust speed (closed orange circles), and simulated wind speed (black line) from the perspective of the Detroit station.

4.1.1 Comparison to Data

In order to gain confidence in this simulation, simulated wind speeds, wind directions, temperature, and reflectivity are compared to observations. Figure 4.1 compares the 10 m wind speed, wind direction, and temperature at Erieau from the simulation and ECCC data at Erieau, and Figure 4.2 compares the 10 m simulated wind speeds with wind speeds from NOAA data at Detroit. While the direction of the observed wind is always between northward and eastward, the simulated wind direction is much more variable, particularly at storm time when the simulated wind is due southeast. Similarly, while the observed temperature is initially similar to the simulated temperature, the temperatures vary more during and after storm-time. There is a clear temperature peak before the storm hits followed by a sharp 5-6°C temperature drop in both sets of data, however this occurs in the simulation nearly 4 hours later than in the observations. While observed and simulated Erieau wind speeds often fall into the same range, higher winds occur in the simulated data up to 12 hours before the storm hits. This is not consistent with observations at Erieau, but it is consistent with both observed and simulated winds at Detroit (Figure 4.2). At storm time, the simulation shows a large peak in wind speed, whereas the peak in observed wind speed is much smaller and occurs 4 hours earlier than the simulated peak. The observed wind speed also shows a second peak of even higher winds not observed in the simulation. However, after the storm, both observed and simulated wind speeds closely match each other. Because the data set of wind speeds at the Erieau station is temporally sparse and does not include gust information, it is difficult to confirm whether the simulated wind speeds during the storm are close to the actual wind speeds.

The Detroit data set can be used to help confirm these unknowns. Comparing winds at Detroit in Figure 4.2, it can be seen that the observed storm peak appears to occur about 3-4 hours before the simulated storm peak, which is consistent with Erieau observations. Observed wind speeds are much higher than simulated wind speeds during the storm, with observed wind gusts over twice as strong as simulated wind speeds. However, wind speeds are remarkably similar before the storm, capturing an earlier wind event and the trend of rising winds before the storm quite well. Winds are observed to be higher than the simulated wind speeds after the storm, which is also consistent with Erieau data. This comparison shows that this simulation captures the overall sustained wind speed of the storm, but dramatically underestimates the wind gusts. Interestingly, the simulation tends to overestimate ECCC wind speed at Erieau and underestimate NOAA wind speed at Detroit during the storm. This could be due to the topography of each area or to the sampling process of NOAA's 1-minute averages versus ECCC's 2-minute averages. The high observed winds at Detroit compared to the simulation provides evidence that the real

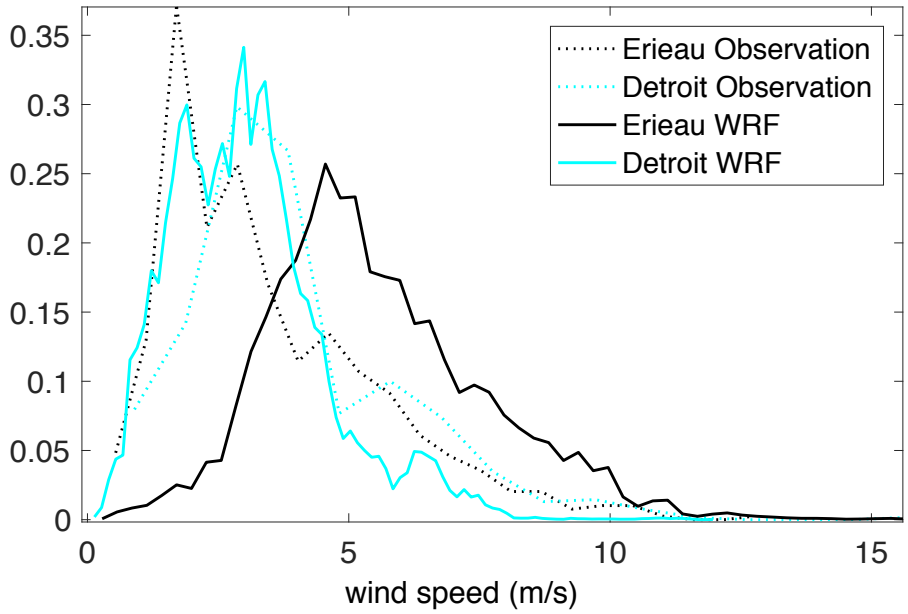

Figure 4.3: The distribution of sustained wind speed obtained from observations (dashed lines) and 2 km resolution simulations (solid lines) from Erieau (cyan) and Detroit (black).

wind gusts at Erieau may be even higher than the simulated wind peak of nearly 27 m/s during the storm.

Figure 4.3 compares July 1998 wind speeds at Erieau and Detroit by showing the distribution of sustained wind speeds for both observed and simulated winds. While their associated Weibull distributions are not shown, the Weibull parameters and means are presented in Table 4.1. The distribution of both simulated and observed wind speeds at Detroit are very similar. In addition, the dashed lines show that the observed winds at Detroit are higher than those at Erieau. Since Detroit samples more frequently during high-wind events, it makes sense that the observed wind speeds at Detroit are shifted higher than observed wind speeds at Erieau. The solid lines show that the simulation produces higher wind speeds at Erieau than it does at Detroit. Since Erieau is next to Lake Erie, wind speeds are expected to be greater. However, there is a large inconsistency between simulated and observed wind speeds at Erieau. This could be due to the sampling at Erieau.

To look closer at how sampling affects data and how simulated and observed wind speed distributions match the structure of a Weibull wind speed distribution, the distribution

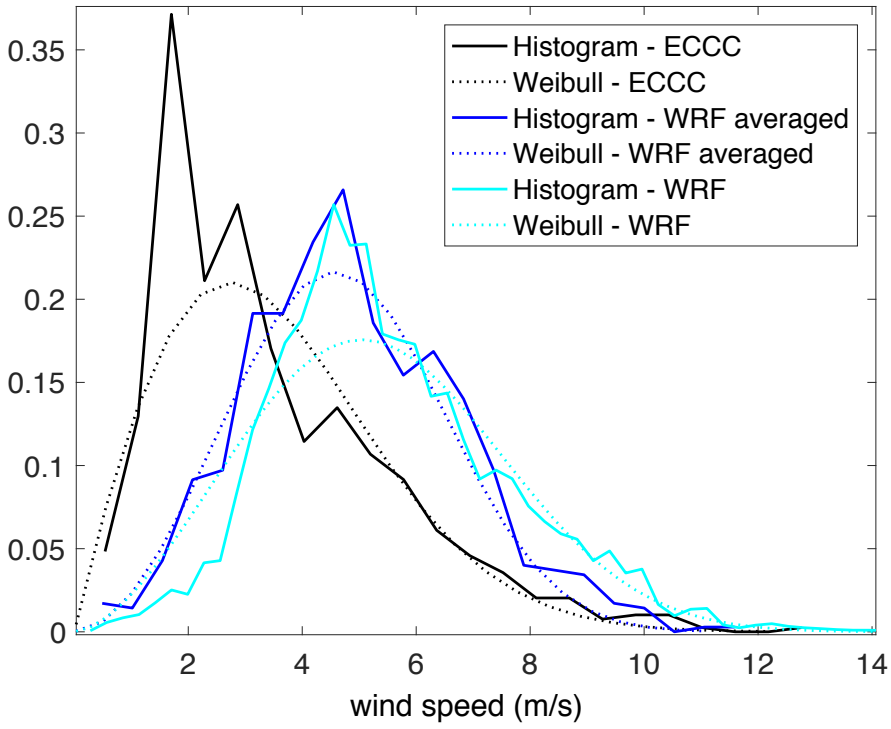

Figure 4.4: Histogram (solid lines) of ECCC data (black), hourly 2-minute averaged 2 km resolution WRF data (blue), and 2 km resolution WRF data (cyan) compared to their estimated Weibull probability distribution function (dashed lines). The month July 1998 and location of Erieau is used for all curves.

Table 4.1: A summary of Weibull scale parameter c, shape parameter k, and mean wind speed for various observed and simulated WRF wind speeds. WRF 2 km resolution wind speeds are averaged using a 2-minute hourly average in line with Erieau's averaging process.

	c (m/s)	k	mean (m/s)
Observations July 1998 - Erieau	4	1.9	3.5
Observations July 1998 - July	4.4	2.1	3.9
Observations 1995-2015 - Erieau	4.9	1.6	4.3
Observations 1995-2015 - Detroit	5	2.1	4.4
WRF July 2 km - Erieau	6	2.7	5.4
WRF July 2 km averaged - Erieau	5.3	2.9	4.7
WRF July 10 km - Erieau 1995-2015	5.3	2.3	4.7
WRF July 2 km - Detroit	3.4	2.2	3.0

of all observed wind speeds in July 2018 from Erieau is compared to the histogram of all simulated wind speeds in Figure 4.4. Both of these are compared to their appropriate Weibull distribution. To account for the loss of information due to ECCC's averaging process, another histogram is created using simulation data averaged with a 2-minute hourly average. Overall, the simulated wind speeds in July are higher than the observed wind speeds, with an average simulated speed of 5.4 m/s compared to an average observed speed of 3.5 m/s. Averaging the simulation's output in the same way as the ECCC data shifts the average down by 0.7 m/s. The simulated wind reaches greater speeds that sampling for only 2 minutes every hour often misses. All curves are accompanied by their appropriate Weibull probability distribution function, fitted using the parameters outlined in Table 4.1. Both simulated curves appear to follow a Weibull distribution closely, while the ECCC curve is shifted towards lower wind speeds than the Weibull curve suggests.

Figure 4.5 shows the simulated and observed reflectivity data at July 22 00:00 UTC. The overall structure of the simulated storm closely matches the structure of the observed storm. There is a clear band of precipitation traveling east over Lake Erie and lower Lake Huron. At this time, the observed storm has propagated further than the simulated storm, which is shown to hit Rondeau Park 3-4 hours later. This is consistent with the one-dimensional wind speed data in Figure 4.1. At this time, there is another smaller storm observed following the initial storm that doesn't appear in simulations, explaining the lack of a second wind speed peak in Figure 4.1. The similar structure of the reflectivity from both the observations and the simulation provides confidence that the overall dynamics of the structure storm can be successfully simulated. However, the lack of a second distinct storm in the simulations shortens the effective length of storm conditions.

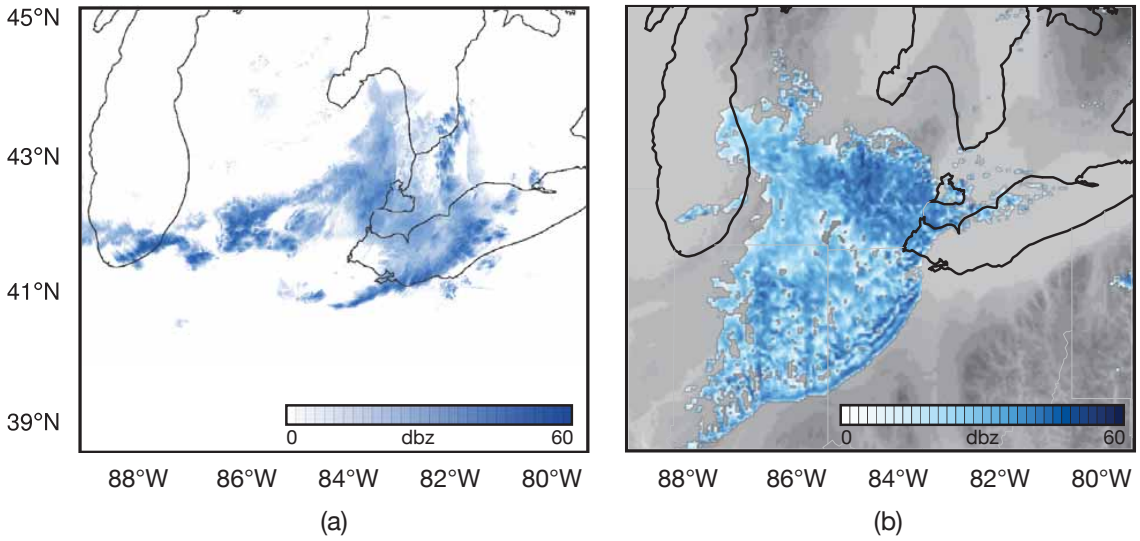

Figure 4.5: Observed (a) and simulated (b) reflectivity (dbz) values at July 22 00:00 UTC. Observations are obtained from NOAA satellite data.

4.1.2 Simulated Storm Characterization

To characterize the simulated storm, the storm-scale 2 km resolution simulation is analyzed. Figure 4.6(b) shows the location of the maximum surface wind speed in the domain for hourly outputs, tracking the course of the storm over 16 hours, while Figure 4.6(a) shows the corresponding wind speed of each point. The storm travels eastward for its entire duration, passing over the Great Lakes of Lake Michigan, Lake Erie, and finally Lake Ontario. The points of maximum wind speed often occur over lakes, including the high wind speeds that occur over Lake Ontario, even as the bulk of the storm moves south of it. Interestingly, the highest wind speed at 01:00 July 22 UTC occurs on Lake St. Clair, indicating stronger winds to the north of Lake Erie. In addition to this, all the maximum wind speeds that occur over Lake Erie occur on the north shore. The highest wind speeds over all outputs occur soon after the storm forms: as the storm approaches and passes over Lake Michigan, it has wind speeds of up to 43 m/s. The wind speeds in the 25-30 m/s range that occur east of Lake Michigan are representative of the simulated wind peak that occurs at Rondeau Park, shown in Figure 4.1.

In the 8 hours prior to the storm, the pressure at Rondeau Park shows a steady drop

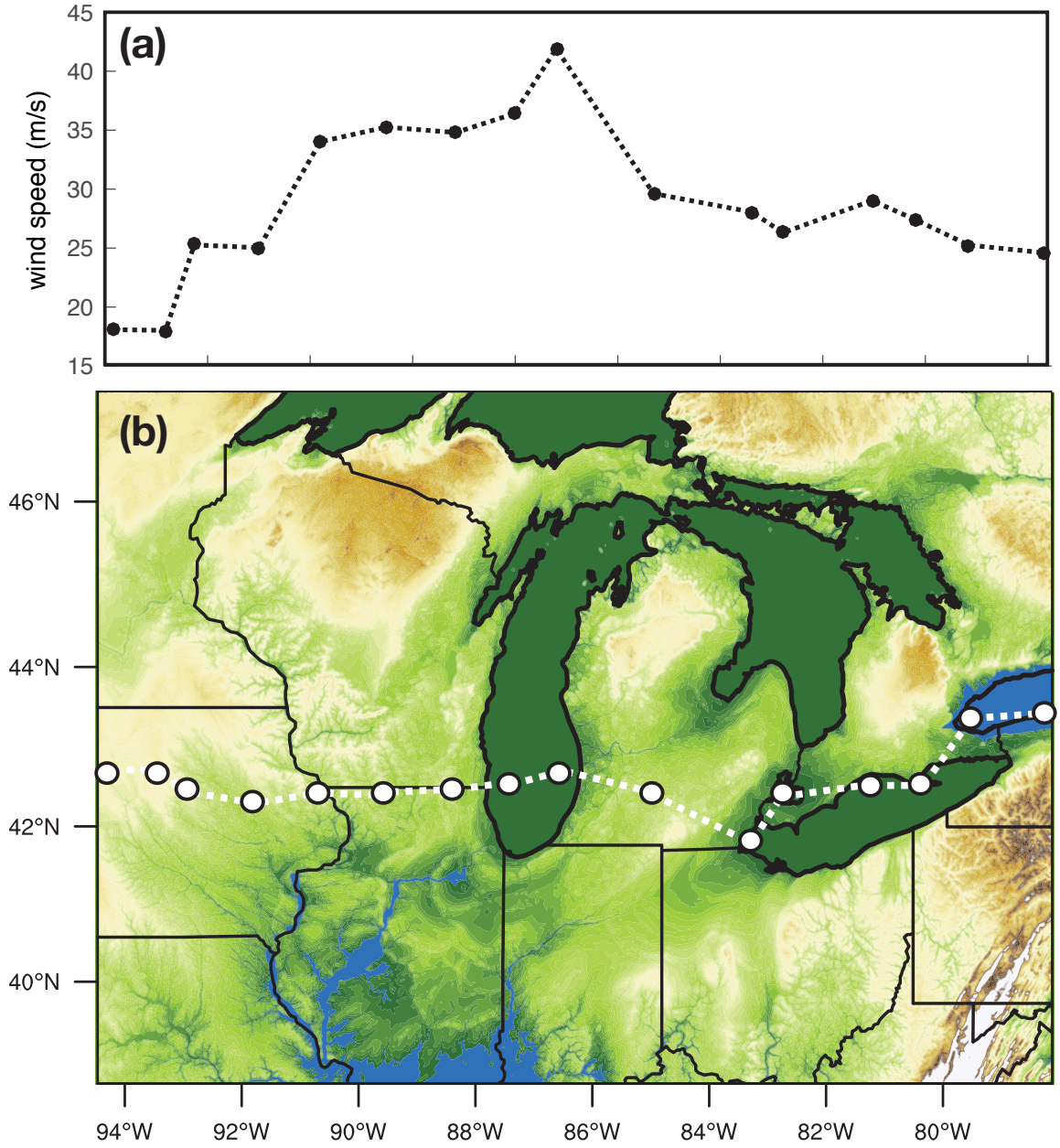

Figure 4.6: Trajectory of the simulated storm based on the location of hourly simulated maximum 10 m wind speed. (a) Maximum wind speed over the domain, and (b) locations of the maximum wind speeds for hourly outputs between July 21 14:00 UTC and July 22 06:00 UTC.

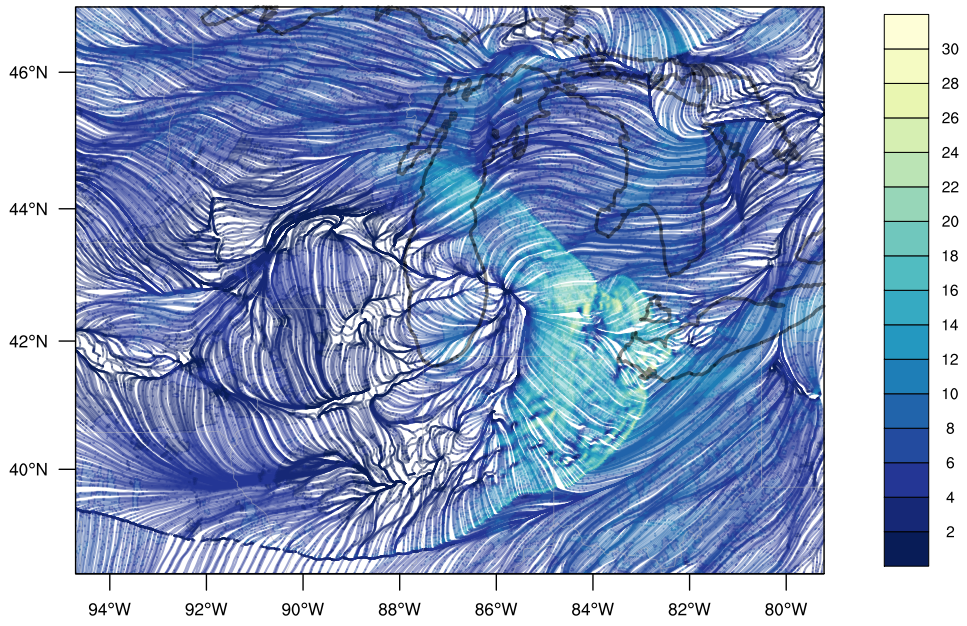

Figure 4.7: Streamlines of simulated 10 m winds, coloured by wind speed (m/s) at July 22 00:00 UTC.

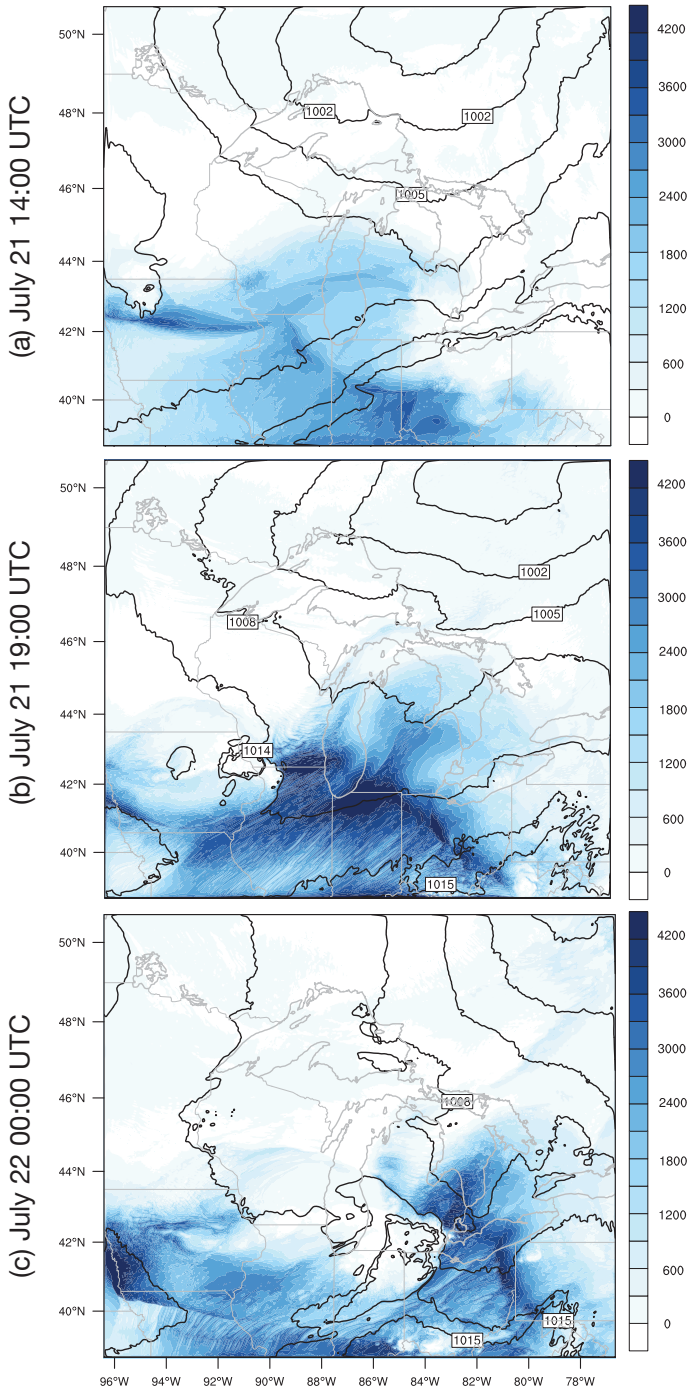

Figure 4.8: Evolution of simulated CAPE (m^2/s^2) with sea level pressure contours (kPa).

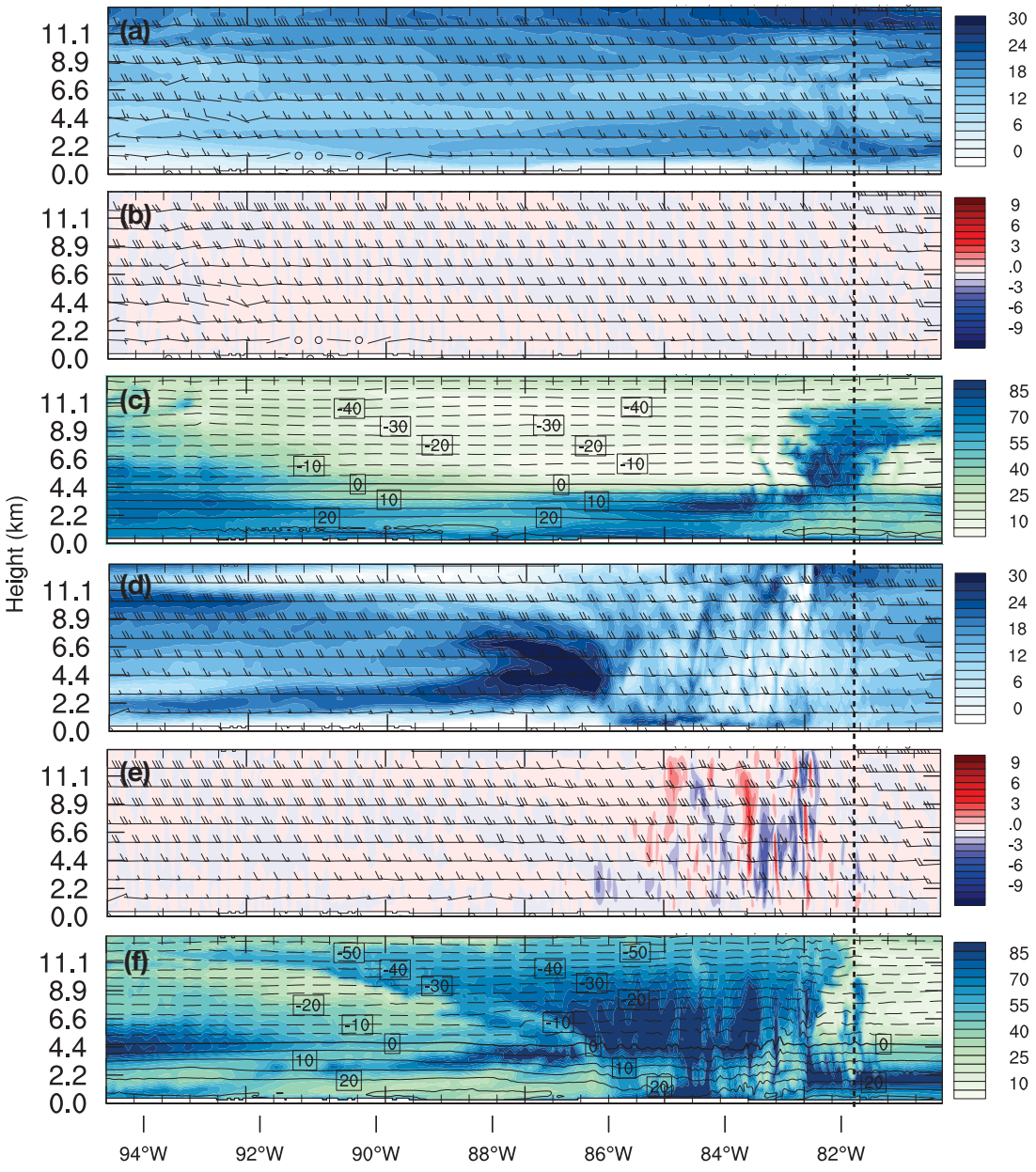

Figure 4.9: Simulated longitude-height cross-sections from before the storm at July 21 16:00 UTC (a-c) and during the storm at July 22 00:00 UTC (d-f). Cross-sections show (a and d) longitudinal wind speed (m/s) with wind direction vectors, (b and e) vertical wind speed (m/s) with wind direction vectors, and (c and f) relative humidity (%) with temperature contours (°C). Slices are through the Erieau station at 42.256 °N, with Rondeau Park denoted as a dashed line.

from 99.3 to 98.75 kPa as the temperature rises from 24 to 28°C, as seen in Figure 4.1. When the storm passes over the park, there is a rapid temperature drop of about 5 degrees and a pressure rise of 0.75 kPa. At this point, the main downburst has spread to about a 250 km radius, estimated from Figure 4.7, and crosses the park heading due east. At this point, the direction of the large-scale atmospheric winds closely matches the direction of the storm-influenced wind gusts, as shown in Figure 4.7. This alignment constructively heightens the wind speeds occurring at the park.

To determine the atmospheric conditions prior to and during the storm, Figure 4.8 shows the simulated sea level pressure and near-surface CAPE present in the domain at July 21 14:00, July 21 19:00, and July 22 00:00 UTC. Prior to the formation of the storm, the future storm path is shown to have rising levels of near-surface CAPE in Figure 4.8(a). As the storm forms and begins to move in the direction of large-scale wind, the CAPE grows larger over the southern Great Lakes, shown in Figure 4.8(b) and (c). The maximum near-surface CAPE in the domain prior to storm formation has a value of 5300 J/kg, and the maximum CAPE in the entire domain is 16500 J/kg. Thus, the atmosphere is severely unstable and has the potential for a large amount of convection. Along with the CAPE present prior to the storm, there is low-level atmospheric wind shear of about 10 m/s over the bottom 3 km of the atmosphere shown in Figure 4.9(a). However, once the storm is formed, a maximum shear of 37 m/s appears within the storm in the bottom 6 km of the atmosphere shown in Figure 4.9(d). This shear, along with the high CAPE, provides ideal conditions for the formation and continuation of strong convection.

Figure 4.9 shows the longitudinal and vertical simulated wind speed, temperature, and relative humidity along longitudinal cross-sections passing through Rondeau Park prior to the storm at July 21 16:00 UTC and during the storm at July 22 00:00 UTC. Figure 4.9(d-f) show the deep, moist convective properties of this storm as it passes over Rondeau Park. When the storm hits the park, the vertical structure of the storm front is tilted rearward, reaching over 10 km in height in an anvil shape. Convection is shown inside the storm as bands of humid and less humid air, collocated with bands of alternating upward and downward velocities as shown in Figure 4.9(f) and (e). It can be noted that the main region of high vertical winds near the front edge of the storm is due to cold air falling as a continuous downburst, shown by a high downward velocity following the leading edge of the storm in Figure 4.9(e), associated with rain and continuing downburst winds. There is a strong and moist temperature gradient in Figure 4.9(f). As the storm travels east, it pushes the initially humid air near the surface up over the storm front. This is followed by a strong longitudinal wind in the mid-levels of the atmosphere in the form of a gravity current, seen in Figure 4.9(d), providing the bulk of the storm with strong kinetic energy.

Figure 4.7 plots the streamlines and speed of the 10 m wind at July 22 00:00 UTC. It

shows that a family of downbursts has formed within and around the main downburst. It can be seen that one of these downbursts appears on the east side of the main storm at around July 22 00:00 UTC. This new downburst occurs almost directly on top of Rondeau Park, which will experience effects of the new burst constructively interfering with the main storm, resulting in the sudden peak of winds in Figure 4.1.

4.2 Coarse Resolution Simulation

Initially, a 2 km resolution was chosen to resolve the convective interactions in the atmosphere. While these simulations effectively resolve the processes present in the atmosphere, they are computationally expensive. To assess the need for a cloud resolving grid and to determine the effects of resolution and convective parameterization, an additional simulation with 10 km resolution is run for the month of July 1998. This simulation, referred to as 10 km July, uses Kain-Fritsch cumulus parameterization described in Section 2.5.1. Simulation parameters are outlined in Table 2.2.

The 10 km July simulation is compared to the 2 km July simulation to determine the effects of grid resolution and convection scheme on general wind speeds present at Erieau. Both sets of simulated wind speeds seem consistently larger than observed wind speeds at Erieau, regardless of the resolution and convection scheme. Figure 4.10 shows the simulated wind speed distribution of both the 2 km July and the 10 km July simulations along with their appropriate Weibull distributions. Weibull parameters and means are listed in Table 4.1. Both curves tend to fit a Weibull distribution with similar heights and widths, where the 2 km resolution simulation is shifted to higher wind speeds. With a grid size of over 6 times larger and a time step of 5 times longer, the 10 km simulation's wind speed is averaged over a a much larger area both spatially and temporally. This averaging brings the strength of the wind speed down in general. As a result, the 10 km simulation has a distribution that is slightly closer to the distribution of ECCC observed wind speeds as opposed to the 2 km resolution simulation. Table 4.1 shows that the 10 km July simulation has an identical mean and similar Weibull parameters as the 2 km July simulation that is averaged as a 2-minute hourly average. Thus, the larger grid spacing and larger timestep act to average the data in a similar way as observed sustained wind averages, missing the smaller scale gusts that act to heighten the mean wind speed.

Along with larger-scale wind trends, it is also important to look at how representative the 10 km resolution simulation is of the storm itself. Figure 4.11(a) shows the CAPE present in the low level atmosphere of the 10 km resolution simulation as the storm approaches Rondeau Park. Contrasting this to Figure 4.11(b) which shows the CAPE present

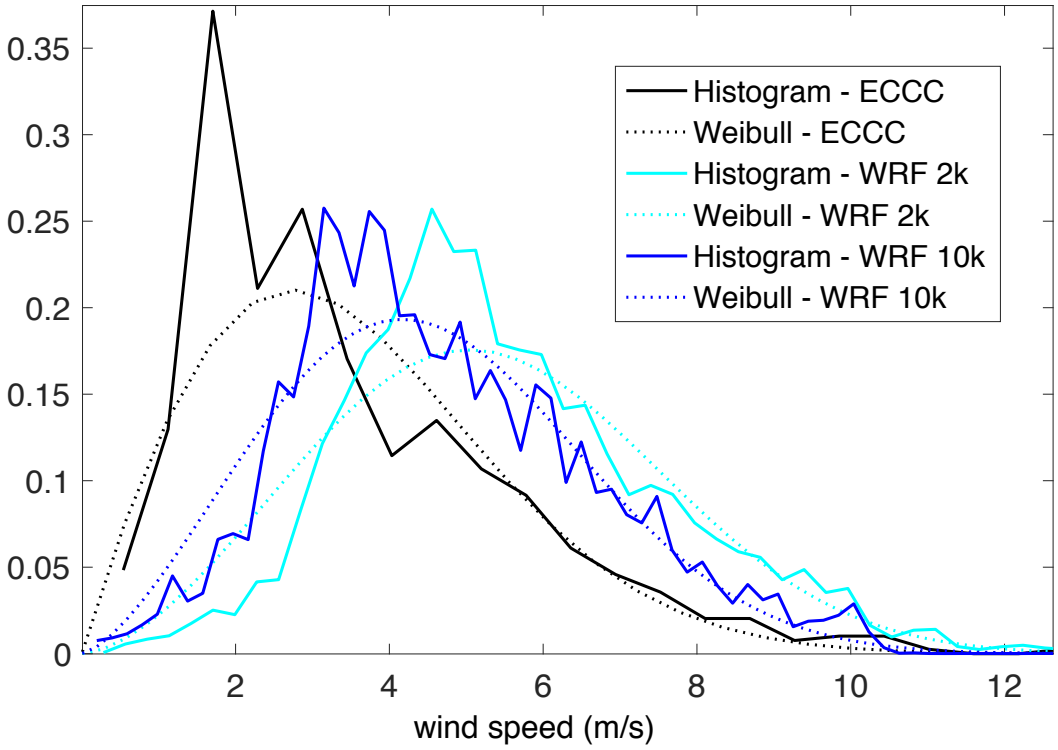

Figure 4.10: Histogram (solid lines) of ECCC wind speeds (black), wind speeds outputted from the 10 km resolution simulation (blue), wind speeds outputted from the 2km resolution simulation (cyan) compared to their estimated Weibull probability distribution function (dashed lines). The month of July 1998 is used for all curves.

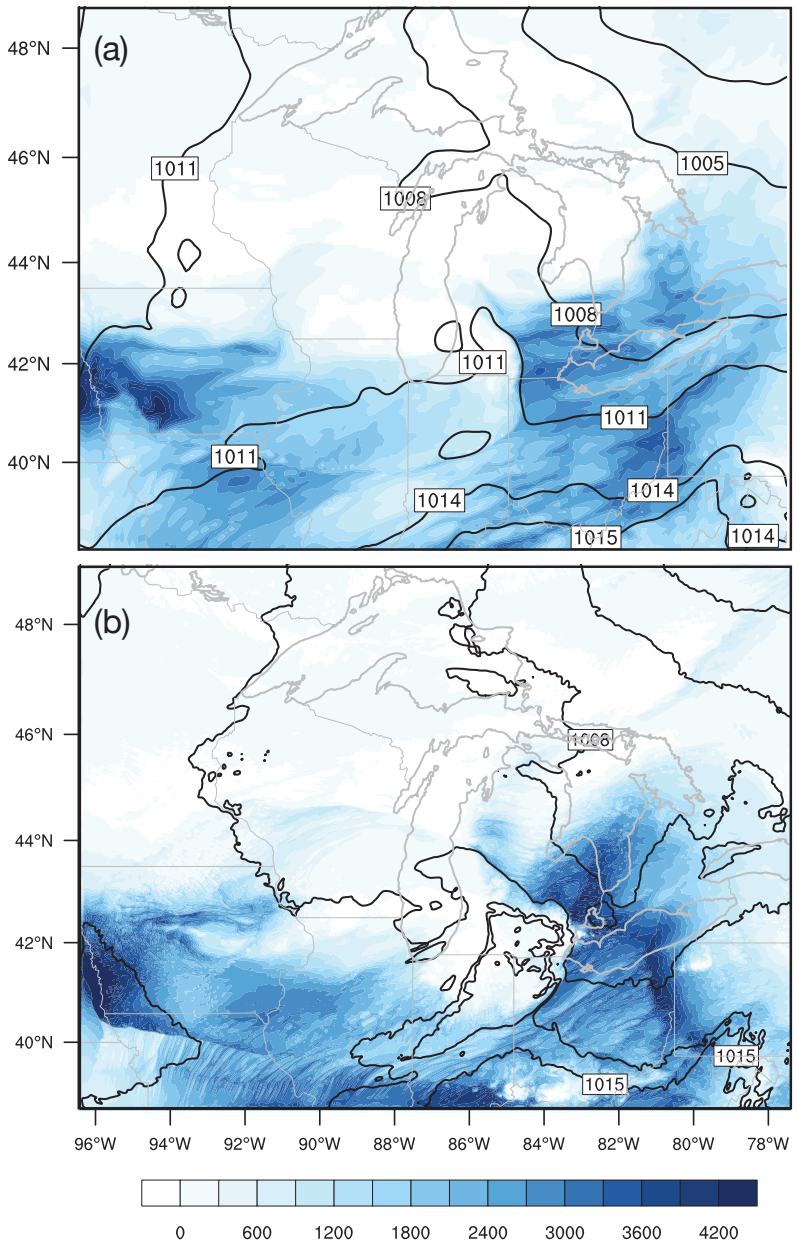

Figure 4.11: Simulated CAPE (m^2/s^2) with sea level pressure contours (kPa) for the 10 km resolution simulation (a) and the 2 km resolution simulation (b) at July 22 00:00 UTC.

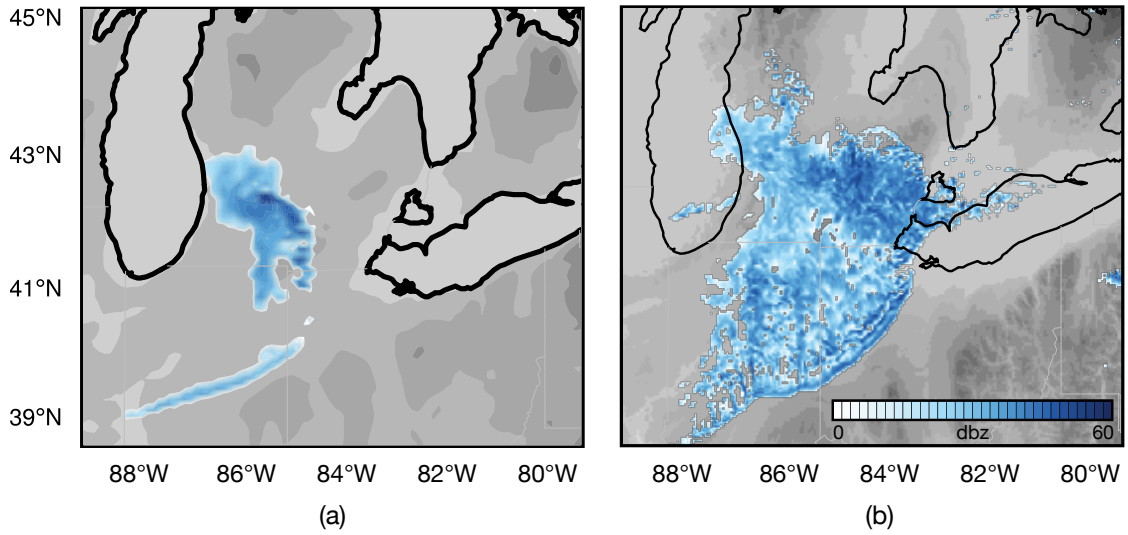

Figure 4.12: Simulated reflectivity (dbz) for the 10 km resolution simulation (a) and the 2 km resolution simulation (b) at July 22 00:00 UTC.

at the same time in the 2 km resolution simulation, it is evident that the finer resolution provides spatial details not present in the coarse resolution simulation. Additionally, the CAPE that exists to the east of the storm (that helps with the propagation of convective activity) is much lower in the coarse resolution simulation than it is in the fine resolution simulation. Similarly, Figure 4.12 shows a comparison between the simulated reflectivity for both the 10 km resolution simulation and 2 km resolution simulation at July 22 00:00 UTC. Not only does the coarse resolution storm appear later than the fine resolution storm (and thus significantly later than the observed storm), it appears to be smaller and less intense. Levels of high reflectivity within the coarse resolution storm are limited to the front of the storm, where reflectivity is not resolved for areas within the storm as it is in the fine resolution simulation.

Figure 4.13 shows the longitude-height cross-sections of longitudinal wind speed (a), vertical wind speed (b), and relative humidity (c) produced by the 10 km resolution simulation. A clear storm front can be seen as a rapid change in relative humidity in panel (c), followed by strong horizontal winds in panel (a). Panel (b) shows that the simulation produces some upwards and downwards motions associated with convection. Contrasting these results to those produced in the 2 km resolution simulation, shown in Figure 4.9(d-f), the significance of the resolution and parameterization on these cross-sectional features can

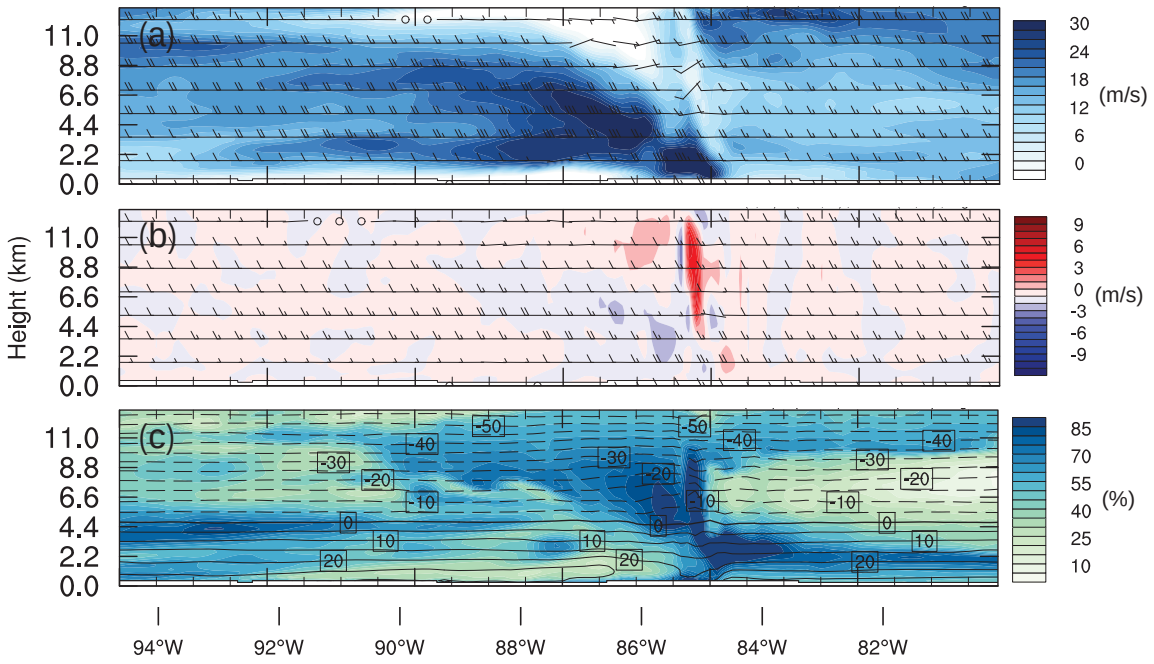

Figure 4.13: Simulated longitude-height cross-sections during the storm at July 22 00:00 UTC. Cross-sections show (a) longitudinal wind speed (m/s) with wind direction vectors, (b) vertical wind speed (m/s) with wind direction vectors, and (c) relative humidity (%) with temperature contours (°C). Slices are through the Erieau station at 42.256°N.

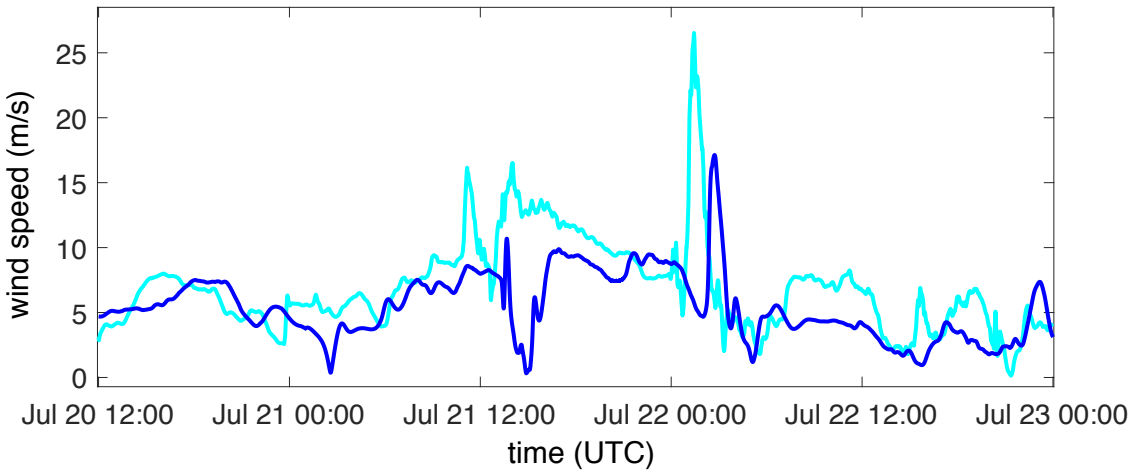

Figure 4.14: Simulated wind speed of the storm for 10 km July (blue) and the initial 2 km resolution simulation (cyan) from the perspective of Rondeau Park.

be determined. The coarse resolution simulation shows similar horizontal wind features as the fine resolution simulation with strong winds moving eastward as a gravity current with the leading edge at 86°W. While the gravity current occurs at nearly the same location at the same time for both simulations, there is a significant difference between the regions of high activity that appear to the east of 86°W. Figure 4.13 depicts the 10 km resolution storm as shorter in spatial extent: the leading edge of the 10 km resolution storm storm is at around 85°W as opposed to around 83°W for the fine resolution storm. It is in this area that the fine resolution storm contains most of its convection-associated updrafts and downdrafts, with at least 5 regions of strong vertical upwards winds alternating with consecutive regions of vertical downwards winds. Although only one significant updraft appears in the coarse resolution storm, followed by the downdraft associated with the gravity current, this is expected due to the parameterization of sub-grid updrafts in the convective scheme. Similarly, the tall vertical region of high humidity associated with cumulus clouds is significantly greater in width in the fine resolution storm. The fine resolution simulation is able to capture a large region of storm activity that the coarse resolution simulation fails to. This is not only clear in the cross sections in Figure 4.13, but in the reflectivity shown in Figure 4.12. This region of high activity in the fine resolution simulation is nearly 160 km greater in length than the coarse resolution simulation, acting to temporally lengthen the wind effects and potential for damage at a single location.

To look at effects of wind speed at Rondeau Park, Figure 4.14 shows the simulated 10 m wind speeds during the storm from both the fine and coarse resolution simulations. Overall, the wind speed simulated by the 10 km resolution simulation is much lower than that simulated by the 2 km resolution. This is consistent with the weaker winds shown in Figure 4.10. The wind speeds differ the most when the storm is present over the park: the length of the storm peak is shorter, and there is nearly a 10 m/s difference in peak wind speed. This is due to the lessened up- and downdrafts acting to dampen horizontal convectively-driven winds. In addition to this, the post-storm wind speeds are much lower. The coarse resolution also simulates the storm nearly 6 hours after it occurs in observations and 2 hours after it occurs in the fine resolution simulation.

While the coarse resolution simulation does provide evidence of a storm and the general shape and location of the storm, where the simulation misses out is in details and intensity. Nearly 160 longitudinal kilometres of active storm area is missing from the coarse resolution simulation. Even with the cumulus parameterization, the coarse resolution simulation fails to capture the strong winds present at the park.

4.3 Impacts of Lake Erie

One of the factors that plays into the strong wind speeds observed at Rondeau Park is the presence of nearby lakes, the surface of which is hydrodynamically smoother than the surrounding land. To determine the magnitude of Lake Erie and Lake St. Clair's effects on the storm, a simulation is performed in which Lake Erie and Lake St. Clair are replaced by surface vegetation. In the WRF preprocessing system, lake variables in a rectangle encompassing both lakes are replaced by the land variables closest to their neighbouring values. In this case, the land use is switched from 'Inland Lake' to 'Evergreen Broadleaf Forest' in this region. These changes affect the land-surface model, surface layer schemes, and planetary boundary layer schemes, simulating an identical domain without the presence of Lake Erie or Lake St. Clair. This simulation will be referred to as Lake Off and will be compared to the original simulation, referred to here as Lake On. Both simulations have identical domains and a 2 km grid resolution. Model setup and parameterizations for both simulations are found in Table 2.2.

Figure 4.15(b) shows the location of the maximum surface wind speed in the domain for hourly outputs, and Figure 4.15(a) shows the corresponding wind speed of each point. Initially, the trajectory of the storm in the Lake Off simulation closely matches the location of the storm in the Lake On simulation. As the storm travels eastward, the maximum wind speed peaks over Lake Michigan, which is still defined as a lake for this simulation. The

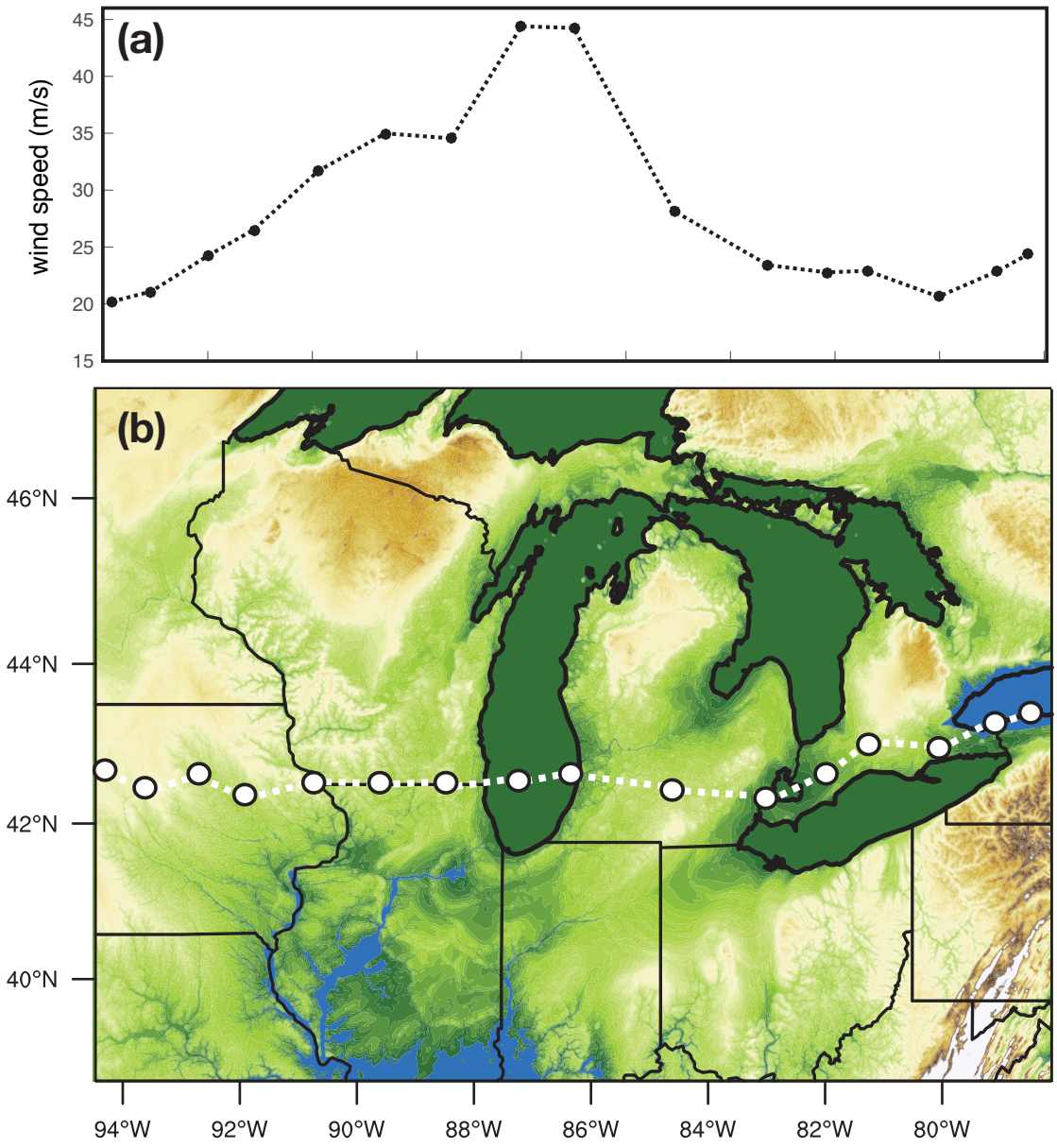

Figure 4.15: Trajectory of the storm in the Lake Off simulation based on the location of hourly simulated maximum 10 m wind speed. (a) Maximum wind speed over the domain, and (b) locations of the maximum wind speeds for hourly outputs between July 21 14:00 UTC and July 22 06:00 UTC.

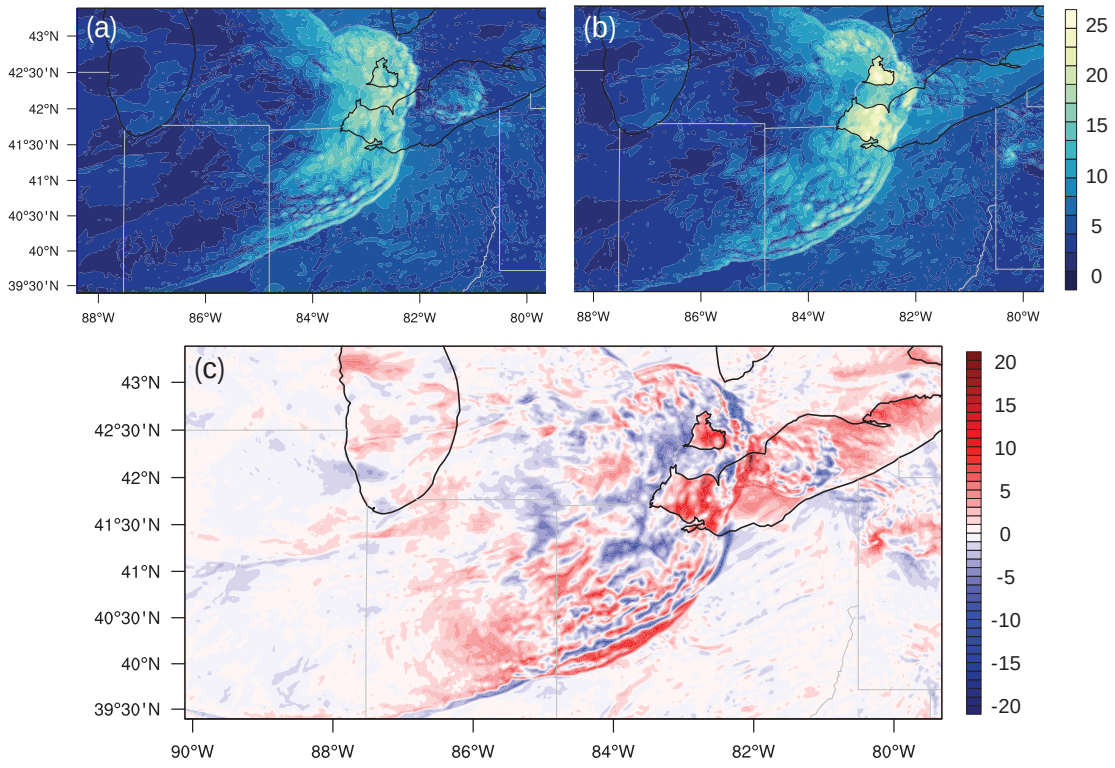

Figure 4.16: Simulated 10 m wind speed (m/s) at 00:00 UTC on July 22 produced by the (a) Lake off and (b) Lake On simulations, and the difference between the 10 m wind speeds (c), calculated by (b) - (a).

maximum wind speeds over Lake Michigan are even greater than those where Lake Erie and Lake St. Clair are present in the domain. After the storm crosses Lake Michigan, wind speeds drop significantly more than the amount they dropped in the Lake On simulation. The path of maximum wind speed crosses just north of where Lake Erie would reside in the domain, near Rondeau Park. It is interesting to note that the region of highest wind speed will occur on the north side of Lake Erie whether or not Lake Erie is defined as a lake.

From the perspective of Rondeau Park, the 10 m winds in the Lake Off simulation are shown in Figure 4.16(a). The storm appears similar in shape and inland intensity to the storm in the Lake On simulation, shown in panel (b) of Figure 4.16. The difference of the 10 m winds is shown in panel (c). The distribution of CAPE (not shown) is unchanged between the two cases. The most obvious change to the 10 m wind distribution in the Lake Off case is the absence of the high wind speeds that appear over the water in the Lake On simulation. Areas where the storm has not hit yet experience higher pre-storm wind speeds with the presence of Lake Erie. These high wind speeds cause the storm to propagate quicker over Lake Erie and move towards Rondeau Park at a faster rate. The sustained wind speeds of the storm itself are higher: at the time of the output shown in Figure 4.16, the maximum 10 m wind speed over the whole domain in the Lake Off simulation subtracted from the maximum 10 m wind speed of the Lake On simulation gives a difference of 3.53 m/s, showing that the storm in general produces higher winds overall in the presence of the lakes. Other outputs in which the storm is prevalent show that the Lake On simulation has a higher wind speed over the lake than the Lake Off; wind speeds consistently reach up to 15 m/s higher over the length of the lake when it is defined to act as water.

Figure 4.17 shows the 10 m wind speed in the Lake On and Lake Off simulations at the location of Rondeau Park. This location experiences higher winds in the Lake On simulation compared to the Lake Off simulation throughout the majority of the simulation. Peak winds from the storm in the Lake On simulation appear at the park earlier than the Lake Off simulation; these peak winds last until after the Lake Off peak winds have subsided. The winds from the lake are a consistently higher speed at times in which the storm is not present. Thus, the presence of the lake significantly impacts the length of the immediate impacts of the storm front as well as the background levels of wind. Because the wind speed fluctuates within the peak of the storm, there is a maximum wind speed difference of 17 m/s between the two simulations, with an average wind speed difference of about 3.5 m/s within the peak winds.

From Figure 4.16, the shape of the storms also differ, with the Lake On simulation propagating quicker and further on top of and south of Lake Erie, however traveling less

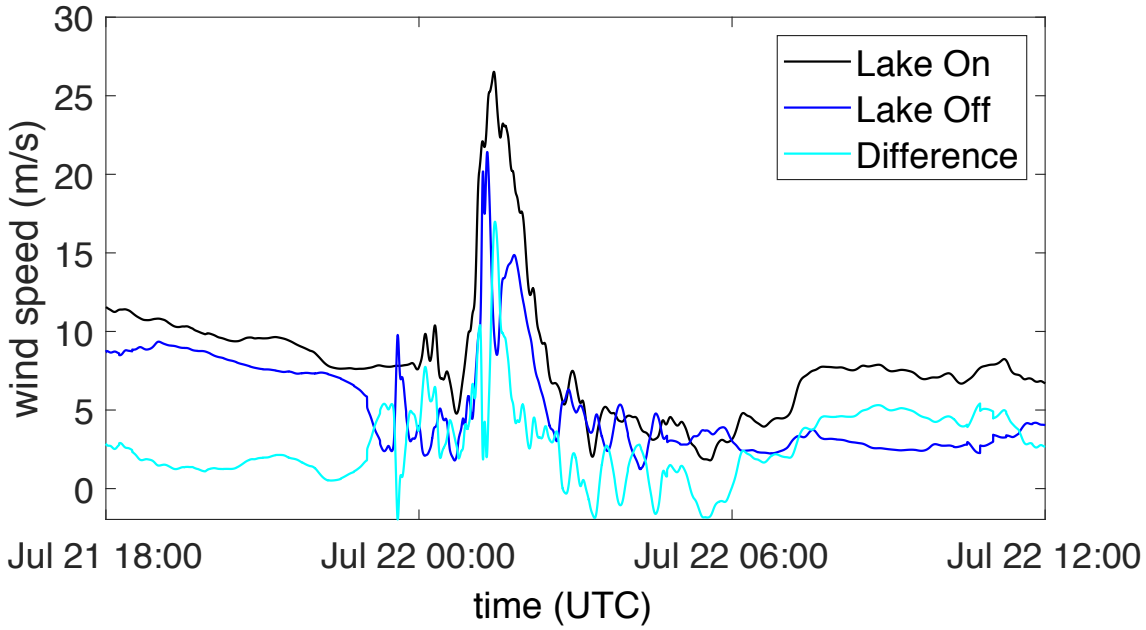

Figure 4.17: Simulated 10 m wind speed (m/s) produced by the Lake On (black) and Lake Off (blue) simulations, and the difference between the 10 m wind speeds (cyan) from the perspective of Erieau.

far in the north, past Lake St. Clair. Thus, the existence of a lake changes more than just the immediate wind speeds directly on the lake, but the shape of the storm, even where the storm does not interact directly with the lake itself.

Chapter 5

Discussion

This thesis focuses on the wind storm of July 21-22 1998. Climatology of the Erieau, Ontario and Detroit, Michigan areas are performed to determine the region's seasonal potential for high winds and sustained wind events. Two storm-scale and two month-scale simulations are performed to assess the following: where the storm fits into the general climate, the effect of cumulus parameteriaztion and resolution on wind speed and storm dynamics, and the effect of lakes on the development and propagation of the storm. Conclusions obtained from both observational analysis and simulations, a discussion on storm damage with regards to tree fall, and potential future research are presented in this chapter.

5.1 Conclusions

The overall storm structure of July 21-22 1998 is consistent with previously determined climatology: it occurs in one of the highest-frequency summer storm corridors, is formed in the afternoon and ends in the early morning along with a large percent of convective storms, and has consistent synoptic-scale systems involved in its formation. Reanalysis data shows that, on the day of the storm, a strong temperature and humidity gradient is present in a region south of a low-pressure zone, aiding in the formation of such a strong convective storm. While it occurs in a month where convective storms are very likely, a sustained wind event in this month with observed high winds in one location lasting over 2 hours, such as this storm, is rare. Over 20 years of wind speed and wind gust data collected in Detroit during the summer, this storm records one of the highest wind speed/gust combinations of 20.6 m/s and 29.5 m/s. Wind gusts observed along the trajectory of the storm aid

in the estimation of gust strength at Erieau specifically, where large sustained winds are observed, but gust strength is not.

A high resolution WRF simulation is used to determine several characteristics about the storm that are impossible to access from measurements alone. Comparing simulation outputs to various observations, it is shown that the simulations correctly capture the basic features of the storm: the simulated reflectivity closely matches the time and extent of the observed storm and the simulated wind speeds are similar to those observed at Detroit and Erieau. However, observed wind speed values at Rondeau Park itself are less consistent with the simulations during the storm. The simulated wind speeds are closer in value to observations from Detroit than they are to observations from Erieau. In both locations, the observed storm occurs 3-4 hours before the simulated storm. Simulations show that high relative humidity and warm surface provide the potential for instability. This is consistent with the large amount of CAPE present in the lower levels of the atmosphere. Once the storm is formed, a low-level shear acts to propagate the storm further spatially and extend its life cycle temporally. The combination of low level moisture, instability, lift, and shear act to cause severe deep moist convection, as described by Johns and Doswell (1992).

A simulation with 10 km resolution and convective parameterization is run for the month of July 1998 to compare with a simulation with 2 km resolution run for the same time period. The general wind speeds outputted in the 2 km resolution simulation are higher than the 10 km wind speeds. However, both simulated wind speeds are higher than those observed and averaged at Erieau and Detroit. The coarse resolution storm not only lacked detail that the finer resolution could provide, but it weakened the CAPE in the region and shrunk the horizontal extent of the storm greatly. The up- and downdrafts parameterized by the convection scheme could not simulate the extent of the vertical winds simulated in the finer resolution, and thus dampen the convectively-driven horizontal winds experienced throughout the storm.

The presence of Lake Erie and Lake St. Clair affected storm propagation as well as the shape and peak wind speed of the storm. When the lakes are present in the simulation, the maximum wind speeds over the domain always occur over lakes when the storm is present over them. However, a high resolution simulation performed with Lake Erie and Lake St. Clair acting as land show that the maximum wind speeds will not occur in the same locations without the lakes present, but rather occur over land masses north of Lake Erie. At Rondeau Park itself, the storm produced up to 17 m/s higher wind speeds during the storm's peak wind gust in the presence of both lakes rather than when the terrain of both lakes is altered to act as land. Thus, the close proximity of Rondeau Park to Lake Erie contributed to the damaging high winds that occurred during this storm.

5.2 Damage Implications

Many atmospheric, forest-scale, and stand-scale factors contributed to the particularly destructive nature of this storm, which damaged over 50% of trees at Rondeau Park. Atmospheric features such as wind speed, precipitation, and turbulence have an obvious role in the destruction of trees in the park (Xi et al., 2008). Too much precipitation causes root instability, and near-surface turbulence causes a back and forth swaying of trees, weakening the trunk. When wind gusts are in-phase with tree sway, trees are more likely to overturn, even in lower winds. The exposed area of the forest next to Lake Erie is a large factor in the strong winds experienced at the park, since winds propagating along the lake will result in higher winds at the park compared to a situation in which the park is surrounded by land (and trees in particular). The transition from open lake to the scattered forests of Rondeau Park results in high wind drag, classified by the Davenport-Wieringa roughness-length classification as "chaotic," with a large aerodynamic roughness length. Thus, high surface winds will result in high friction velocities, corresponding to large stress on the trees (Stull and Ahrens, 2000).

Major tree fall events occur due to a number of non-atmospheric properties, ranging from the stand-scale wood strength, crown size, extent and depth of root system, biomechanical stem properties (Asner and Goldstein, 1997) to forest-scale properties such as forest age, height, density, exposure, elevation, slope, and soil type Xi et al. (2008). It was mid to large sized trees that saw the most damage during this storm (Larson and Waldron, 2000), which is in line with previous studies that have claimed mid-sized diameters of around 50 cm have the highest probability of uprooting in Carolinian forests (Xi et al., 2008). Larson and Waldron (2000) claim that the combination of sandy soil, dead crown branches, root rot from a high water table, and the previous exposure to storms in the area play the largest role in the treefall of July 21-22 1998. Based on 10 years of data, El Niños have been followed by a high number of derechos across the US in May, June, and July. In particular, the El Niño of 1998 saw many more derechos in May and June (Ashley, 2005). Analysis of reanalysis and radar data in July 1998 show that two weaker convective storms hit the area on July 19 and 20, 1998. These storms provided the forest with little recovery time before the major storm of interest hit on July 21 1998.

Both natural and human disturbances in forests are only expected to get worse as the climate changes: increased precipitation, increased chance of drought, insect and pathogen outbreaks, and introduced species could all act to weaken the health of a forest as a whole Dale et al. (2001). In combination with the predicted increased intensity and frequency of convective wind storms (Berz, 1993), damage to forests could be even more severe in the future. Modelling storms can help determine which prediction strategies are useful in pre-

dicting storms with given atmospheric conditions. Modelling convective wind storms will also provide us with information on storm intensity within a region, helping to determine which topographies are most sensitive to damage within these types of storms. This in turn helps to pinpoint areas which may need further wind damage mitigation techniques as storms are strengthened with climate change.

5.3 Future Work

The work presented in this thesis provides a basis for potential future research, whether specific to this particular storm, other storms, or general climate analysis. While characteristics of the July 1998 storm are presented in detail, an additional set of simulations could be performed to provide sensitivity analysis regarding a number of issues. Firstly, the lake sensitivity analysis presented in Chapter 4.3 suggests more ways to consider a number of land use changes. For instance, Figure 4.6 shows that the wind speed of the storm picks up by a large amount over Lake Michigan. An additional simulation could be run in which Lake Michigan is represented by forest instead of water variables. This would determine if and how the presence of Lake Michigan acts to propagate the storm, and whether the lake affects the strength of the storm later on at Rondeau Park. Additionally, a simulation could be run in which the entirety of the Great Lakes are set as nearby land-use variables instead of water. In addition to how the storm acts over multiple modified regions, this simulation could determine if the moisture from the Great Lakes is needed in the evolution of the storm, or if the moisture in the initial state and from lateral boundary forcing is enough to form a sizable storm.

Representing a lake as a forest changes a number of parameters that could influence storm generation and propagation. Most evident in the simulations is the change in surface roughness that contributes to lower winds. However, the presence of a lake introduces other features, such as moisture fluxes and a cooler surface, that could also play a role in storm dynamics. By carefully representing several parameters discussed in Section 2.5.2, it is possible to isolate these different surface parameters in several simulations. By doing so, this study could be expanded upon by determining how each different lake parameter affects the storm.

In addition to lake sensitivity analysis, simulations could be performed to provide the sensitivity of a simulation to parameterization changes. For instance, it would be interesting to see the effects of a cumulus parameterization in finer grids, since cumulus paramerizations may act to help trigger convective motions even in finer resolution grids that can resolve updrafts and downdrafts (Skamarock et al., 2008). Additionally, a very

high resolution simulation on the order of 100 m could be performed in order to resolve boundary layer turbulence without the need for a planetary boundary layer scheme, as well as explicitly resolve convection. This could provide insight into the variation of wind speeds near the surface and the extent of convectively-produced downdrafts.

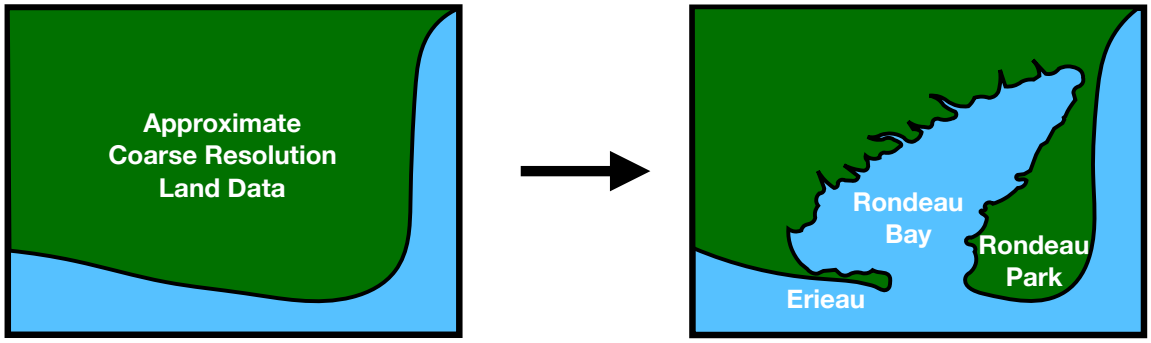

Figure 5.1: The approximate area representing Rondeau Park as determined by WRF geography data versus the actual region of Rondeau Park, Rondeau Bay, and Erieau.

It is worth noting that the resolution of the geographical land data itself is too coarse to show details of the Erieau region. Figure 5.1 shows the region as represented by WRF along with a depiction of the actual region. By finding or constructing finer resolution land data, at least in the region, a more detailed look at how the Erieau peninsula, bay, and sandspit that makes up Rondeau Park act together to strengthen or weaken winds in the area. This could determine whether the presence of Rondeau Bay in between two masses of land influences the turbulence of air in the boundary layer, thus affecting the influence of wind on tree sway.

Additionally, it was stated in Section 2.3 that reanalysis data is not entirely observational and thus may produce uncertainties. As the initial and boundary conditions for the simulations in this study are produced with reanalysis data, it is important to take into account how these uncertainties contribute to uncertainties within the simulations. By choosing one starting time and boundary location, the simulation is determined by a small set of possibly inconsistent reanalysis data. However, an ensemble averaging approach may be used to minimize these consistencies. This can be achieved by running a larger set of simulations, each with slightly different initial and boundary conditions, and averaging the output. While this approach is computationally expensive, it would provide this study with a better idea of the average dynamics of the storm, and how representative a single simulation can be of this average.

Finally, this study can be expanded upon not just by looking at this single storm, but by expanding the study to multiple storms in the lower Great Lakes region. By picking a location, a date range, and a threshold wind speed or gust speed, a set of high-wind events can be identified. Radar data can be used to determine if these high-wind events are part of a bigger storm. For instance, every storm in the summer months of June, July, and August with sustained wind speeds greater than a threshold of 15 m/s could be identified. Modelling and comparing the characteristics and effects of the storm could help provide an in-depth climatology of regions that cannot be described with observational data alone.

References

Arakawa, A. The cumulus parameterization problem: Past, present, and future. *Journal of Climate*, 17(13):2493–2525, 2004.

Ashley, W. S. *Derecho-Producing Convective Systems in the United Stated: An Assessment of Hazards and Family Formation*. Doctoral dissertation, University of Georgia, 5 2005.

Asner, G. P. and Goldstein, G. Correlating stem biomechanical properties of Hawaiian canopy trees with hurricane wind damage. *Biotropica*, 29(2):145–150, 1997.

Babanin, A. V. and Makin, V. K. Effects of wind trend and gustiness on the sea drag: Lake George study. *Journal of Geophysical Research: Oceans*, 113:1–18, 2008.

Bentley, M. L. and Mote, T. L. A climatology of derecho-producing mesoscale convective systems in the central and eastern United States. part i: Temporal and spatial distribution. *Bulletin of the American Meteorological Society*, 79(11):2527–2540, 1998.

Berz, G. A. Global warming and the insurance industry. *Interdisciplinary Science Reviews*, 18(2):120–125, 1993.

Colle, B. A. and Mass, C. F. The February 1996 flooding event over the Pacific Northwest: Sensitivity studies and evaluation of the MM5 precipitation forecasts. *Monthly Weather Review*, 128(3):593–617, 2000.

Coniglio, M. C., Stensrud, D. J., and Richman, M. B. An observational study of derecho-producing convective systems. *Weather and Forecasting*, 19(2):320–337, 2004.

Coniglio, M. C., Correia, J., Marsh, P. T., and Kong, F. Verification of convection-allowing WRF model forecasts of the planetary boundary layer using sounding observations. *Weather and Forecasting*, 28(3):842–862, 2013.

Dale, V. H., Joyce, L. A., McNulty, S., Neilson, R. P., Ayres, M. P., Flannigan, M. D., Hanson, P. J., Irland, L. C., Lugo, A. E., Peterson, C. J., Simberloff, D., Swanson, F. J., Stocks, B. J., and Wotton, B. M. Climate change and forest disturbances: Climate change can affect forests by altering the frequency, intensity, duration, and timing of fire, drought, introduced species, insect and pathogen outbreaks, hurricanes, windstorms, ice storms, or landslides. *BioScience*, 51(9):723–734, 2001.

Done, J., Davis, C. A., and Weisman, M. The next generation of NWP: explicit forecasts of convection using the weather research and forecasting (WRF) model. *Atmospheric Science Letters*, 117(September):110–117, 2004.

Doswell, C. A. I., editor. *Extreme Convective Windstorms: Current Understanding and Research*, volume 8 of *11*, Barcelona, Spain, 6 1993. Spain-U.S. Joint Workshop on Natural Hazards.

Dudhia, J. Numerical study of convection observed during the winter monsoon experiment using a mesoscale two-dimensional model. *Journal of the Atmospheric Sciences*, 46(20): 3077–3107, 1989.

Dudhia, J. A history of mesoscale model development. *Asia-Pacific Journal of Atmospheric Sciences*, 50(1):121–131, Jan 2014.

Dyer, A. J. and Hicks, B. B. Flux-gradient relationships in the constant flux layer. *Quarterly Journal of the Royal Meteorological Society*, 96(410):715–721, 1970.

Emanuel, K. A. *Atmospheric Convection*. Oxford University Press, 1994. ISBN 0195066308, 9780195066302.

Flesch, T. K. and Reuter, G. W. WRF model simulation of two Alberta flooding events and the impact of topography. *Journal of Hydrometeorology*, 13(2):695–708, 2012.

Fujita, T. Manual of downburst identification for project nimrod. *Satellite and Mesometeorology Research Paper*, 156, 06 1978.

Golden, J. H. and Snow, J. T. Mitigation against extreme windstorms. *Reviews of Geophysics*, 29(4):477–504, 1991.

Hong, S.-Y. and Lim, J.-O. J. The WRF single-moment 6-class microphysics scheme (WSM6). *J. Korean Meteor. Soc*, 42(2):129–151, 2006.

Hong, S.-Y., Dudhia, J., and Chen, S.-H. A revised approach to ice microphysical processes for the bulk parameterization of clouds and precipitation. *Monthly Weather Review*, 132 (1):103–120, 2004.

Hong, S.-Y., Noh, Y., and Dudhia, J. A new vertical diffusion package with an explicit treatment of entrainment processes. *Monthly Weather Review*, 134(9):2318–2341, 2006.

Johns, R. H. Meteorological conditions associated with bow echo development in convective storms. *Weather and Forecasting*, 8(2):294–299, 1993.

Johns, R. H. and Doswell, C. A. Severe local storms forecasting. *Weather and Forecasting*, 7(4):588–612, 1992.

Johns, R. H. and Hirt, W. D. Derechos: Widespread convectively induced windstorms. *Weather and Forecasting*, 2(1):32–49, 1987.

Kain, J. S. The Kain-Fritsch convective parameterization: An update. *Journal of Applied Meteorology*, 43(1):170–181, 2004.

Kundu, P. and Cohen, I. *Fluid Mechanics*. Elsevier Science, 2010. ISBN 9780123814005.

Laprise, R. The Euler equations of motion with hydrostatic pressure as an independent variable. *Monthly Weather Review*, 120(1):197–207, 1992.

Larson, B. M. H. and Waldron, G. E. Catastrophic windthrow in Rondeau Provincial Park, Ontario. *Canadian Field-Naturalist*, 114(1):78–82, 2000.

Lawson, J. and Horel, J. Ensemble forecast uncertainty of the 1 December 2011 Wasatch windstorm. *Weather and Forecasting*, 30(6):1749–1761, 2015.

Lin, Y.-L. *Mesoscale Dynamics*. Cambridge University Press, 2007. ISBN 10.1017/CBO9780511619649.

Litta, A. J., Mohanty, U. C., and Idicula, S. M. The diagnosis of severe thunderstorms with high-resolution WRF model. *Journal of Earth System Science*, 121(2):297–316, 2012.

Maddox, R. A. Mesoscale convective complexes. *Bulletin of the American Meteorological Society*, 61(11):1374–1400, 1980.

Mesinger, F., DiMego, G., Kalnay, E., Mitchell, K., Shafran, P. C., Ebisuzaki, W., Jovi, D., Woollen, J., Rogers, E., Berbery, E. H., Ek, M. B., Fan, Y., Grumbine, R., Higgins, W., Li, H., Lin, Y., Manikin, G., Parrish, D., and Shi, W. North American regional reanalysis. *Bulletin of the American Meteorological Society*, 87(3):343–360, 2006.

Mlawer, E. J., Taubman, S. J., Brown, P. D., Iacono, M. J., and Clough, S. A. Radiative transfer for inhomogeneous atmospheres: RRTM, a validated correlated-k model for the longwave. *Journal of Geophysical Research: Atmospheres*, 102(D14):16663–16682, 1997.

Parker, W. S. Reanalyses and observations: Whats the difference? *Bulletin of the American Meteorological Society*, 97(9):1565–1572, 2016.

Paulson, C. A. The mathematical representation of wind speed and temperature profiles in the unstable atmospheric surface layer. *Journal of Applied Meteorology*, 9(6):857–861, 1970.

Rogers, R. *A Short Course in Cloud Physics*. International series in natural philosophy. Pergamon Press, 1976. ISBN 9780080196947.

Schoen, J. M. and Ashley, W. S. A climatology of fatal convective wind events by storm type. *Weather and Forecasting*, 26(1):109–121, 2011.

Sharma, A., Fernando, H. J., Hamlet, A. F., Hellmann, J. J., Barlage, M., and Chen, F. Urban meteorological modeling using WRF: a sensitivity study. *International Journal of Climatology*, 37(4):1885–1900, 2017.

Skamarock, W., Klemp, J., Dudhia, J., Gill, D., Barker, D., Wang, W., and Powers, J. A description of the Advanced Research WRF version 3. *NCAR Technical Note NCAR/TN-475+STR*, 2008.

Stephens, G. L. Radiation profiles in extended water clouds. I: Theory. *Journal of the Atmospheric Sciences*, 35(11):2111–2122, 1978.

Stucki, P., Dierer, S., Welker, C., Gmez-Navarro, J. J., Raible, C. C., Martius, O., and Brnnimann, S. Evaluation of downscaled wind speeds and parameterised gusts for recent and historical windstorms in Switzerland. *Tellus A: Dynamic Meteorology and Oceanography*, 68(1):31820, 2016.

Stull, R. and Ahrens, C. *Meteorology for scientists and engineers*. Brooks/Cole, 2nd ed edition, 2000. ISBN 0534372147.

Tanentzap, A. J., Bazely, D. R., Koh, S., Timciska, M., Haggith, E. G., Carleton, T. J., and Coomes, D. A. Seeing the forest for the deer: Do reductions in deer-disturbance lead to forest recovery? *Biological Conservation*, 144(1):376–382, jan 2011.

Tuller, S. E. and Brett, A. C. The characteristics of wind velocity that favor the fitting of a Weibull distribution in wind speed analysis. *Journal of Climate and Applied Meteorology*, 23(1):124–134, 1984.

Webb, E. K. Profile relationships: The log-linear range, and extension to strong stability. *Quarterly Journal of the Royal Meteorological Society*, 96(407):67–90, 1970.

Weibull, W. A statistical distribution function of wide applicability. *Journal of Applied Mechanics*, 18:293–297, 1951.

Weisman, M. L., Skamarock, W. C., and Klemp, J. B. The resolution dependence of explicitly modeled convective systems. *Monthly Weather Review*, 125(4):527–548, 1997.

West, G. L. and Steenburgh, W. J. Influences of the Sierra Nevada on intermountain cold-front evolution. *Monthly Weather Review*, 139(10):3184–3207, 2011.

Wright, D. M., Posselt, D. J., and Steiner, A. L. Sensitivity of lake-effect snowfall to lake ice cover and temperature in the Great Lakes region. *Monthly Weather Review*, 141(2): 670–689, 2013.

Xi, W., Peet, R. K., Decoster, J. K., and Urban, D. L. Tree damage risk factors associated with large, infrequent wind disturbances of Carolina forests. *Forestry: An International Journal of Forest Research*, 81(3):317–334, 2008.

Zhu, L., Jin, J., Liu, X., Tian, L., and Zhang, Q. Simulations of the impact of lakes on local and regional climate over the Tibetan Plateau. *Atmosphere-Ocean*, pages 1–10, 2017.

APPENDICES

Appendix A

WRF Setup

A.1 Altering Land Data

One may wish to modify the type of land in a region (ie. turn lakes into forest) for sensitivity testing. To do so, change the value of `LU_INDEX` for this region in `geo_em.d01.nc` after `geogrid.exe` is run, but before `metgrid.exe` is run. Load the NetCDF Operators module (nco) and use the netCDF Arithmetic Processor (ncap2) to modify `LU_INDEX`. Land use type is given by the USGS 24-category system with an extra category for inland lakes (category 28). For example, to change the land type to grassland in a rectangular region `x1` to `x2` and `y1` to `y2`, type:

```
ncap2 -O -s 'LU_INDEX(:,y1:y2,x1:x2)=7;' geo_em.d01.nc geo_em.d01.nc,
```

where `-O` is to overwrite the original `geo_em.d01.nc` file.

To change a body of water to land, other variables in this region must also be altered:

- Change `LANDMASK` from 0 (water) to 1 (land).
- Change `LAKE_DEPTH` to 10 (default).
- Change `SOILTEMP` to 280.
- Change `SCB_DOM` and `SCT_DOM` to neighbouring soil values.
- Change `LANDUSEF` from 1 to 0 at soil category 20:
  `ncap2 -O -s 'LANDUSEF(:,20,y1:y2,x1:x2)=0;' geo_em.d01.nc geo_em.d01.nc`

- Change `SOILCBOT` and `SOILCTOP` from 1 to 0 at category 13, similar to `LANDUSEF`.

You will also need ensure the following line is in namelist.input so that real.exe will not overwrite surface inputs:

`surface_input_source = 3`.

A.2 Using WPS to plot Reanalysis data

One way to plot large-scale atmospheric features on a domain of interest is to use WPS to superimpose GriB reanalysis data onto a geographical domain. WPS is built to combine reanalysis data and geographical data; you will not need to run WRF itself. Download the appropriate data (eg. NARR data) and set up `namelist.wps` to describe your domain and the time range you wish to see. Run `ungrib.exe`, `geogrid.exe`, and `metgrid.exe`. You will use the `met_em.d01.YYYY-MM-DD-HH:00:00.nc` file to plot the values. In your plotting program of choice, read whichever variables of interest at time 0. For instance, to use `ncl` to plot sea level pressure, type:

`slp = a->PMSL(0,:,:)`,
and create a desired plot of reanalysis data.